An Enhanced PIRATA Dataset for Tropical Atlantic Ocean–Atmosphere Research

GREGORY R. FOLTZ, CLAUDIA SCHMID, AND RICK LUMPKIN

NOAA/Atlantic Oceanographic and Meteorological Laboratory, Miami, Florida

(Manuscript received 17 November 2016, in final form 17 November 2017)

ABSTRACT

The Prediction and Research Moored Array in the Tropical Atlantic (PIRATA) provides measurements of the upper ocean and near-surface atmosphere at 18 locations. Time series from many moorings are nearly 20 years in length. However, instrumental biases, data dropouts, and the coarse vertical resolutions of the oceanic measurements complicate their use for research. Here an enhanced PIRATA dataset (ePIRATA) is presented for the 17 PIRATA moorings with record lengths of at least seven years. Data in ePIRATA are corrected for instrumental biases, temporal gaps are filled using supplementary datasets, and the subsurface temperature and salinity time series are mapped to a uniform 5-m vertical grid. All original PIRATA data that pass quality control and that do not require bias correction are retained without modification, and detailed error estimates are provided. The terms in the mixed-layer heat and temperature budgets are calculated and included, with error bars. As an example of ePIRATA's application, the vertical exchange of heat at the base of the mixed layer (Q_{-h}) is calculated at each PIRATA location as the difference between the heat storage rate and the sum of the net surface heat flux and horizontal advection. Off-equatorial locations are found to have annual mean cooling rates of 20–60 W m^{-2}, while cooling at equatorial locations reaches 85–110 W m^{-2} between 10° and 35°W and decreases to 40 W m^{-2} at 0°. At most off-equatorial locations, the strongest seasonal cooling from Q_{-h} occurs when winds are weak. Possible explanations are discussed, including the importance of seasonal modulations of mixed-layer depth and the diurnal cycle.

1. Introduction

The tropical Atlantic has a strong seasonal cycle that is shaped by coupled ocean–atmosphere–land interactions (Mitchell and Wallace 1992; Okumura and Xie 2004). Deviations of sea surface temperature (SST) and winds from the seasonal cycle, though less pronounced than seasonal changes, are important because of their influence on the location of the intertropical convergence zone (ITCZ) (Nobre and Shukla 1996; Chiang et al. 2002), continental rainfall (Nobre and Shukla 1996; Polo et al. 2008; Yoon and Zeng 2010), and anomalous SST and atmospheric circulation in other ocean basins (Kucharski et al. 2007; Rodríguez-Fonseca et al. 2009; Ham et al. 2013).

The Prediction and Research Moored Array in the Tropical Atlantic (PIRATA) was established in 1997 to improve our understanding and predictability of tropical Atlantic weather and climate (Servain et al. 1998; Bourlès et al. 2008). The array was designed to sample the two main patterns of interannual–decadal variability: the Atlantic meridional mode (Nobre and Shukla 1996; Chiang and Vimont 2004) and the Atlantic equatorial mode (Zebiak 1993; Carton and Huang 1994). Three moorings were added to PIRATA in 2005 as the southwest extension, followed by four additional northeast extension moorings in 2006–07, and a southeast extension mooring at 6°S, 8°E that was first deployed during 2006–07 (Rouault et al. 2009) and then from 2013 to the present (Fig. 1). The scientific motivation for these extensions includes the connection between tropical Atlantic SST and hurricane activity (Kossin and Vimont 2007), the potential impact of the salinity-induced barrier layer on hurricanes and tropical Atlantic climate (Breugem et al. 2008; Reul et al. 2014), the importance of South Atlantic SSTs for South American rainfall variability (Bombardi et al. 2014), and persistent coupled climate model biases (Richter and Xie 2008).

Measurements from PIRATA have been used to address a variety of research topics, including the Equatorial Undercurrent, the upper-ocean diurnal cycle, and tropical instability waves at 0°, 23°W (e.g., Grodsky et al. 2005; Giarolla et al. 2005; Wenegrat and McPhaden 2015); carbon parameters and the factors affecting CO$_2$ variability at 6°S, 10°W (e.g., Parard et al. 2014; Lefèvre et al. 2016); seasonal variations of salinity and their potential impact on

---

Corresponding author: gregory.foltz@noaa.gov

DOI: 10.1175/JCLI-D-16-0816.1

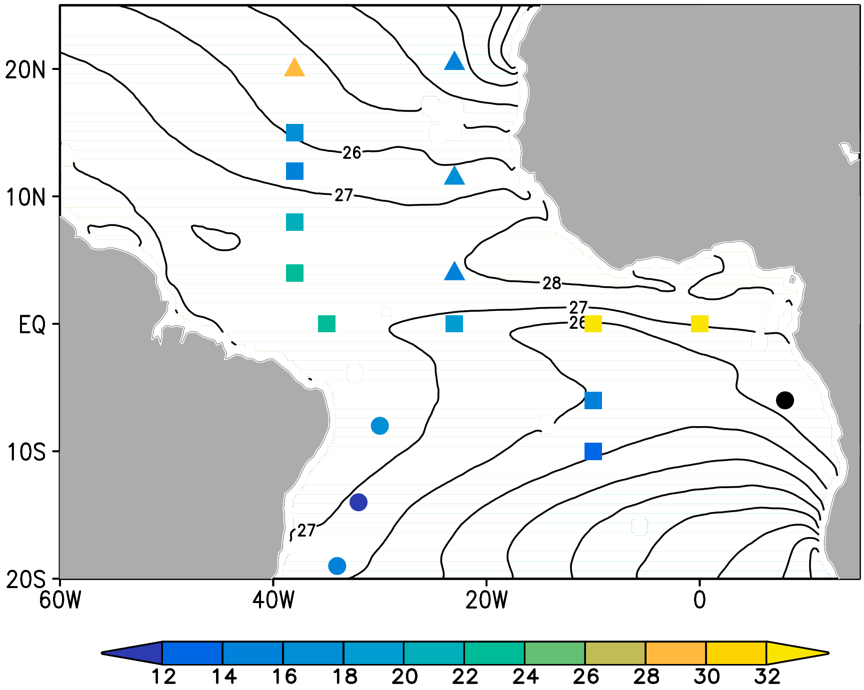

FIG. 1. Annual mean satellite microwave SST (contours, °C). Locations of the "backbone" PIRATA array, first deployed in 1997 (squares). Position of the northeast extension (triangles) and southwest extension moorings (circles), first deployed in 2005–06. Position of the southeast extension mooring (black circle), part of PIRATA since 2013 and not used in this study because of its short duration. Colors indicate the percentage of PIRATA data that are missing at each location, calculated using all sensors and starting on the first day of the first deployment at a given location.

SST (e.g., Foltz and McPhaden 2009; Foltz et al. 2015); and the causes of seasonal and interannual variations of SST (e.g., Foltz et al. 2003, 2012, 2013a; Rugg et al. 2016). PIRATA data have also been used to validate satellite-based measurements of SST (Gentemann et al. 2004), rainfall (Serra and McPhaden 2003), and winds (Ebuchi et al. 2002), and for validation of numerical model output and atmospheric and oceanic reanalyses (e.g., Han et al. 2008; Wade et al. 2011; Nobre et al. 2012).

The time series from many PIRATA moorings are approaching 20 yr in length and are a valuable resource for examining upper-ocean and near-surface atmospheric variability on diurnal to decadal time scales. The moorings' sensors are calibrated after every buoy recovery (approximately once per year) and are regularly quality controlled, yet instrumental biases can remain, and there are some gaps in the time series as a result of sensor failure or other unforeseen circumstances (Fig. 1; appendix; see http://www.pmel.noaa.gov/tao/drupal/disdel/ for full details of data availability). In addition, the vertical resolutions of the subsurface temperature and salinity measurements from the moorings are often too coarse to resolve fully the mixed layer depth and vertical salinity structure, key parameters that affect ocean–atmosphere variability. Since the first PIRATA moorings were deployed in 1997, many new satellite, reanalysis, and in situ datasets have become available (e.g., Argo, ERA-Interim, microwave SST, satellite sea surface salinity) that can be used to fill gaps in PIRATA time series and to provide enhanced vertical resolution of PIRATA temperature and salinity data.

In the remainder of the paper, we describe a new "enhanced" PIRATA dataset (ePIRATA) that provides rigorously quality-controlled, gap-filled (temporal and vertical) time series for ocean–atmosphere research and model validation in the tropical Atlantic. ePIRATA complements the tropical Atlantic components of global datasets, such as TropFlux (Praveen Kumar et al. 2012), OAFlux (Yu and Weller 2007), Argo (www.argo.ucsd.edu/Gridded_fields.html), and the Ocean Surface Currents Analyses–Real Time (OSCAR; Bonjean and Lagerloef 2002), which use in situ measurements from moorings only for validation or to adjust satellite and reanalysis data for biases. Here, in contrast, we retain all original mooring data after quality control and fill gaps with other in situ data and bias-corrected satellite and reanalysis products, forming high-quality continuous daily records, with error bars, at each of the 17 PIRATA locations with a record length of at least seven years. Also included in ePIRATA are continuous daily time series of terms in the mixed-layer heat and temperature budgets at each mooring location, which we anticipate will be useful for exploring the mechanisms of SST variability and the causes of biases in climate models. After describing the methods used to create ePIRATA, we use the dataset to calculate the mixed-layer heat budget residuals at the mooring locations and to relate them to annual mean and seasonal variations of vertical turbulent cooling at the base of the mixed layer.

2. Data and methods

In this section, we describe the data and methods used to create ePIRATA, beginning with the atmospheric parameters and followed by the oceanic data. All moorings measure subsurface temperature and conductivity (used to calculate salinity), as well as air temperature, relative humidity, shortwave radiation, winds, and rainfall. Several moorings also measure barometric pressure, downward longwave radiation, and ocean velocity at a depth of 10 m (Table 1). All data except rainfall and barometric pressure are used in this study. We exclude these variables because they are not used directly to calculate the mixed-layer heat and temperature budgets, one of the main motivations for ePIRATA. Additionally, because of the short time scales and small spatial scales associated with tropical rainfall, filling gaps with gridded datasets is more challenging (Serra and McPhaden 2003). All PIRATA data used in this study are the daily averages, available in real-time online (www.pmel.noaa.gov/tao/disdel/frames/main.html). Higher-temporal-resolution data are also available from the moorings, but they are not available in real time and sometimes not for several years following a deployment. For this reason, and because the coarse vertical resolutions of temperature and salinity on many moorings cannot resolve well the diurnal cycle, we use only the daily-averaged data. Note that any corrections applied to the high-resolution delayed-mode data after postrecovery calibration have also been applied to the daily-averaged data.

a. Atmospheric data

As mentioned in the previous section, biases can develop in the PIRATA time series during approximately yearlong buoy deployments. The first steps are therefore to remove data that are obviously biased and to fill temporal gaps in the records.

1) AIR TEMPERATURE, RELATIVE HUMIDITY, AND WINDS

To determine the quality of the air temperature data, we first create a daily climatology of the difference between SST and air temperature (ΔT) using all available data from a given mooring. We also compute the daily standard deviation of ΔT with respect to its climatology. Because biases very rarely develop in ocean temperature measurements (Freitag et al. 1999), most biases in ΔT can be attributed to issues with the air temperature sensors. The advantage of using ΔT instead of air temperature itself is that ΔT exhibits much smaller variability outside of the seasonal cycle than air temperature. For example, there are noticeable interannual variations in air temperature at many locations, but interannual variations in ΔT are much smaller (Fig. 2a). We focus on identifying data with a spurious long-term drift over at least one month because 1) this is the dominant source of error and 2) biases in shorter-frequency variability are very difficult to detect.

TABLE 1. PIRATA locations with LWR and 10-m ocean velocity measurements. Locations with LWR also measure barometric pressure. Second and third columns indicate beginning years for longwave and velocity measurements, respectively. All measurements continue through the present. Numbers in italics indicate that the data are contaminated by dust.

	LWR	Vel
20°N, 38°W	*2011*	2007
15°N, 38°W	2006	2005
20.5°N, 23°W		2007
11.5°N, 23°W	*2007*	2006
4°N, 23°W		2006
0°, 23°W	2006	2005
10°S, 10°W	2006	2005
19°S, 34°W	2010	

First, for each day at a given location, we count the number of days in a centered 31-day window that have ΔT less than the daily climatology minus one standard deviation (N_l) or greater than the climatology plus one standard deviation (N_h). A period of 31 days was chosen to focus on removing spurious drifts that last longer than one month. Next, the 0.15 and 0.85 quantiles of N_h and N_l are calculated for each calendar day (Q_{15} and Q_{85}, respectively), and days when $N_h > Q_{85}$ or $N_l < Q_{15}$ are flagged as periods when there may be biases in the air temperature measurements. Finally, for a 101-day moving window centered on each day, if the number of days with low flags or high flags is greater than 50, then the flagged values are removed from the record. This step is then repeated with a 301-day moving window and a threshold of 90 days instead of 50. We found, after experimentation, that using a 101-day window with a threshold of 50 gave reasonably robust identification of obviously biased air temperature data. Using fewer days resulted in the elimination of too much data because of some periods with large high-frequency

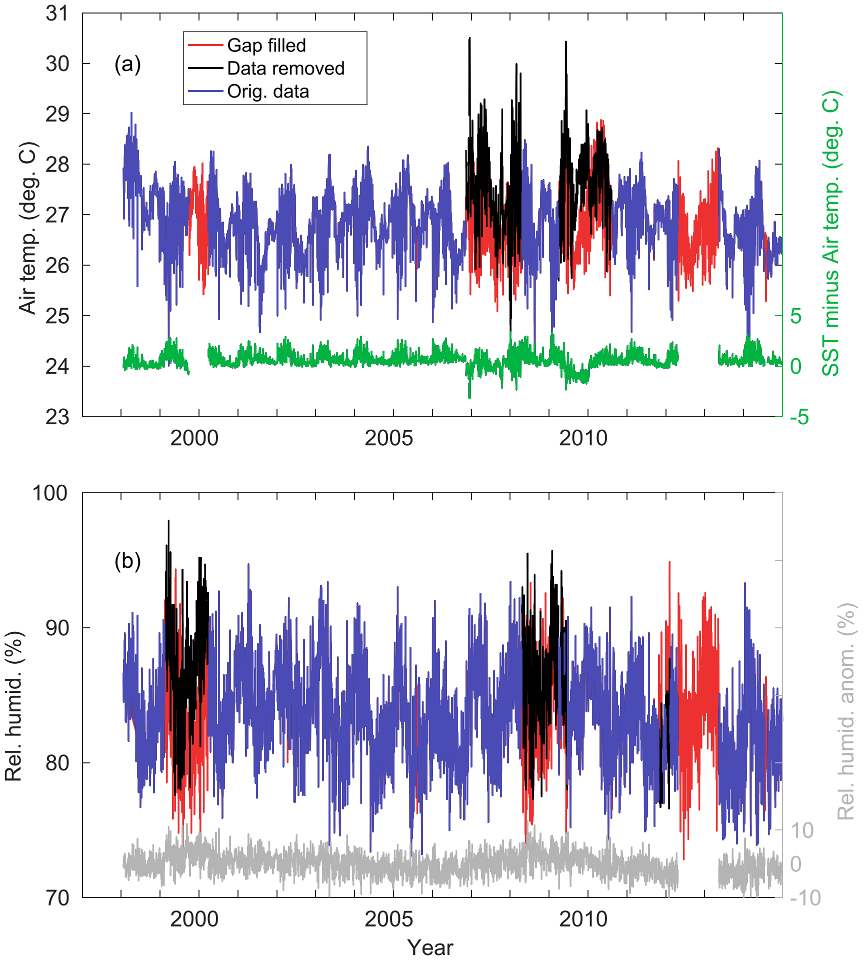

FIG. 2. (a) Time series of original PIRATA air temperature (purple), original data that were removed after quality control (black), bias-corrected ERA-Interim data that were used to fill gaps in the quality-controlled time series (red), and difference between SST and air temperature (green) at 0°, 35°W. (b) As in (a), but for relative humidity (purple, black, and red) and relative humidity anomaly from the daily climatology (gray).

fluctuations of the air–sea temperature difference. Also, because of natural high-frequency variations of the temperature difference, it is necessary to use a longer period of 301 days to identify biases that are small at first and become larger over several months.

This procedure results in up to 5% of the data being removed at each location. Additional subjective quality control is performed based on the ΔT time series, resulting in the total removal of up to 35% of the data at a given location. The subjective procedure mainly involves identifying whole buoy deployments, typically 1–2 yr in length, with questionable data that were not entirely removed by the objective method. As an example, the 0°, 35°W mooring record contains highly questionable data during the deployment from late 2006 to early 2008 and from early 2009 to mid-2010 (Fig. 2a). All of these data were removed, regardless of whether they were flagged by the objective method. Removal was motivated mainly by the presence of sustained negative ΔT values, which were not observed except during these deployments. It is unclear what causes these biases during some deployments, especially since instrumental errors are only about 0.2°C based on predeployment and postrecovery calibration coefficients (Lake et al. 2003). It is possible that something became stuck on the temperature sensor while deployed on the buoy, reducing airflow and hence increasing the temperature the sensor recorded.

To verify that periods of several months with air temperature greater than SST are unrealistic, we calculated the monthly air–sea temperature difference at each PIRATA location from the International Comprehensive Ocean–Atmosphere Data Set (ICOADS; Woodruff et al. 2011) during 1960–2007. We found that 0%–0.7%

of the months at each location have air temperature greater than SST for that month and the following four months. In the monthly TropFlux dataset, during 1979–2015 at each location there are at most three months total, and at most two consecutive months, with air temperature greater than SST, and the differences are always less than 0.1°C. The questionable values of air temperature that we remove from PIRATA records are well outside of these bounds in terms of magnitude and duration.

The same procedure is used to quality control the relative humidity time series from the moorings, except the climatological value is subtracted from the observations to derive the daily anomalies that are used for the detection of biases. This approach results in the removal of up to 5% of the data at each location, except 15% of the data at 0°N, 35°W (Fig. 2b). No data were removed from the PIRATA wind records because no obviously biased values were found. Any remaining gaps in the mooring air temperature, relative humidity, and wind time series were filled with the mooring climatology plus daily ERA-Interim (Dee et al. 2011) anomalies. The mooring and ERA-interim climatologies were calculated using the same periods. Praveen Kumar et al. (2012) found that ERA-Interim near-surface air temperature, humidity, and winds generally agree best with mooring values compared to other reanalysis products. Detailed comparisons at each PIRATA location are provided in the appendix. We use only ERA-interim anomalies from the seasonal cycle in order to eliminate possible annual mean and seasonally varying biases. Note that ERA-Interim does not assimilate PIRATA measurements.

2) SHORTWAVE AND LONGWAVE RADIATION

The main source of error in PIRATA shortwave radiation measurements is the buildup of dust and other aerosols on the radiometer domes at buoy locations north of 4°N (Foltz et al. 2013b). These time-dependent biases are removed following the "MERRA clear sky" method described in Foltz et al. (2013b). Gaps in the time series are filled following the methodology of Praveen Kumar et al. (2012) as follows. For each buoy time series, we first form a daily climatology. We then regress daily NOAA satellite outgoing longwave radiation (OLR) anomalies at the buoy location onto the bias-corrected PIRATA shortwave anomalies. The regression coefficients are applied to the time series of OLR anomalies to create an OLR-based shortwave radiation anomaly time series that is used to fill gaps in the PIRATA time series. The method works reasonably well in the regions where high cloudiness dominates (south of 20°N and outside of the cold tongue region), with daily and monthly anomaly correlations of 0.5–0.8 between the PIRATA shortwave radiation and the OLR-regressed values (Fig. 3). In regions where low cloudiness is more important (e.g., 20°N, 38°W; the eastern equatorial Atlantic; and 6°S and 10°S along 10°W), correlations are generally lower (0.3–0.4). Note that these correlations are for anomalies from the mean seasonal cycle and that the correlations between the full time series range from 0.67 to 0.92, as described in the appendix.

Downward longwave radiation is recorded on six PIRATA buoys (Table 1). At four locations with long records that are unbiased by dust (indicated in Table 1), downward radiation from the moorings is used, and gaps are filled with the daily PIRATA climatology plus the ERA-Interim daily anomalies. At these locations, the correlations between daily anomalies of PIRATA and ERA-Interim downward longwave radiation are between 0.43 (at 10°S, 10°W) and 0.66 (at 19°W, 34°W). Full correlations and RMS differences, calculated with data that include the seasonal cycle, are shown in the appendix. At all other locations, downward longwave radiation directly from ERA-Interim is used. Outgoing surface longwave radiation is calculated as $\epsilon\sigma T^4$, where $\epsilon = 0.97$, σ is the Stefan–Boltzmann constant, and T is SST from the gap-filled PIRATA record (the methodology used to fill gaps is described in the next section).

b. Oceanic data

The oceanic measurements from the PIRATA moorings consist of temperature, salinity, and velocity. At all locations, temperature is available at depths of 1 and 20 m; at 20-m intervals down to 140 m; and at 180, 300, and 500 m. Many moorings have additional sensors in the upper 40 m. Salinity is available at 1, 20, 40, and 120 m at all moorings, and many have additional measurements in that depth range. Velocity is available from some moorings at a depth of 10 m (Table 1 shows the locations). In this section we describe the methodologies used to remove questionable PIRATA data, to fill temporal gaps, and to perform vertical interpolation.

1) TEMPERATURE AND SALINITY

We found no obvious biases in the mooring temperature and velocity time series, based on comparisons between mooring and satellite SST data and an examination of the PIRATA time series for discontinuous jumps or suspicious linear trends during deployments, so no data were removed from them. Gentemann et al. (2004) also did not find any obviously biased SST mooring data in their comparison to microwave SST. For salinity, instrumental bias is most easily detected by examining time series of differences in salinity between depth levels. The first step in the quality-control procedure is therefore calculating differences between the PIRATA salinity from all available depth pairs (ΔS) for

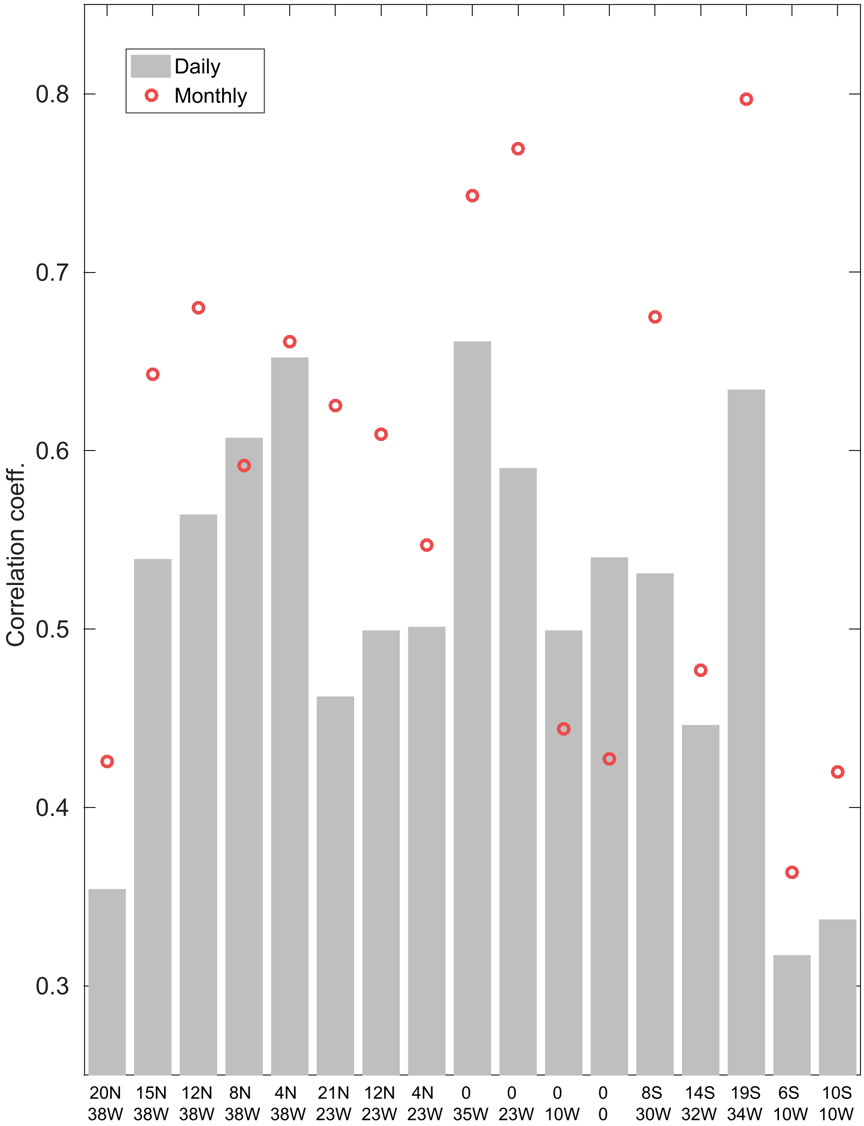

FIG. 3. Correlation between PIRATA SWR and SWR estimated from OLR. Values were computed using anomalies from either the daily mean (gray bars) or monthly mean seasonal cycle (red circles). No smoothing was applied to the time series before computing anomalies. See the appendix for correlations between time series that include the seasonal cycle.

every day in a given record. The full set of depth pairs includes all pairs of unique depths, using only the depths at which salinity measurements are available. For example, on a given day if salinity is available at depths of 1, 20, 40, and 120 m, there are six depth pairs [(1, 20), (1, 40), (1, 120), (20, 40), (20, 120), (40, 120)]. The available depths and depth pairs can be different on different days because of missing data and occasionally the deployment of new sensors during a servicing cruise. From these ΔS values, 3-month seasonal means (January–March, etc.) and standard deviations are calculated for each depth pair. These are used to test whether data on a given day for a given pair of depths are questionable. As before, a moving 31-day window centered on each day in a given PIRATA record is used. If all 31 values of ΔS for a given depth pair exceed the seasonal mean plus three standard deviations or are lower than the seasonal mean minus three standard deviations, then the 31 values at each depth level are flagged. This procedure is repeated for all depth pairs. The flagged data are examined and obviously biased measurements are discarded.

The most obvious indicator of erroneous data is a near-surface salinity inversion (i.e., values that decrease

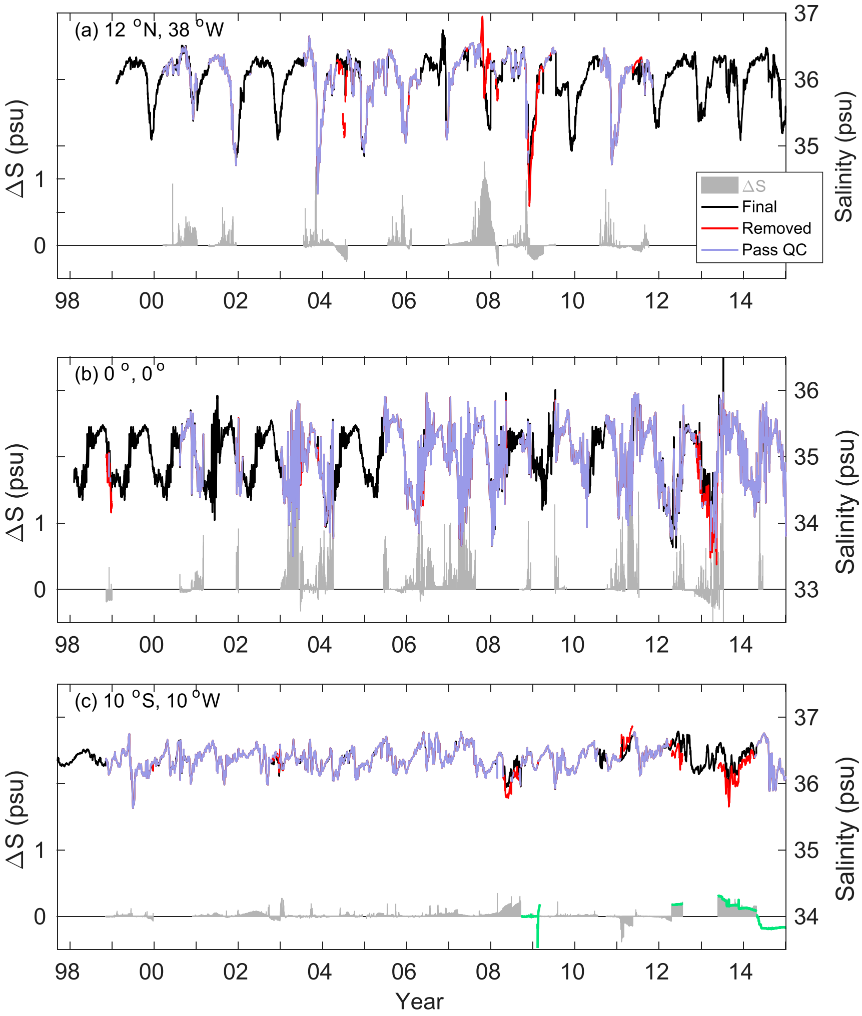

FIG. 4. (a) Daily time series of salinity at a depth of 20 m (purple, red, and black) and the difference between salinity at 20 and 1 m (gray shading) at the 12°N, 38°W PIRATA location. Original PIRATA data that have passed quality control (purple). Data that were removed during quality control (red), and final 20-m salinity record with gaps filled (black). (b) As in (a), except data are from the 0°, 0° mooring. (c) As in (a), except data are from the 10°S, 10°W mooring and salinity is at a depth of 1 m (purple, red, and black); difference between salinity at a depth of 10 and 1 m (green).

with depth) that is not supported by strong temperature stratification, or surface salinity that is abnormally fresher than salinity at a deeper level for an extended period of time. As examples, instances of salinity inversions were found at 12°N, 38°W during 2004 and 2008–09; at 0°, 0° during 2012–13; and at 10°S, 10°W during early 2011 (Fig. 4). Periods with abnormally low salinity at 1 m compared to 20 m were also found at 12°N, 38°W during late 2007 and at 10°S, 10°W during 2008 and 2013–14 (Figs. 4a,c). In many cases, it is easy to label the abnormally fresh values as erroneous because the fresh bias with respect to the next depth immediately disappears when the mooring is serviced and new sensors are installed. Such servicing occurred in April 2008 at 12°N, 38°W (Fig. 4a) and in September 2008 at 10°S, 10°W (Fig. 4c). Overall, this quality-control procedure results in the removal of up to 6% of the salinity data at each location. Resulting gaps in PIRATA surface salinity after July 2011 are filled using the daily climatology from the mooring plus daily anomalies from the Aquarius satellite instrument. This method works reasonably well at most locations (see the appendix for more details). Aquarius data are available from online (http://podaac.jpl.nasa.gov/aquarius) beginning in August 2011 and continuing through May 2015. We anticipate that surface salinity from the *Soil Moisture Ocean Salinity* (*SMOS*) satellite sensor will be useful for filling gaps in future updates to ePIRATA. Gaps in PIRATA SST are filled with microwave satellite SST, available starting in 1998 from online (http://www.remss.com/measurements/sea-surface-temperature/oisst-description) using a similar methodology.

Next, historical Argo profiles are used to map each daily PIRATA temperature and salinity profile to a uniform 5-m resolution in depth. We first obtain all Argo temperature and salinity profiles within ±2° of latitude and ±3° of longitude of a given PIRATA mooring, and within ±90 days of a given calendar day. For example, for 1 April 2010, all profiles available during January–June of any year are obtained. We then interpolate each Argo profile to a 5-m vertical grid, from 10 to 200 m, and extend it upward to 5 and 1 m using the value at 10 m. The assumption of a uniform layer from 1 to 10 m is reasonable because we are using daily-averaged PIRATA data. There are between 390 and 1605 profiles available for the regression at each PIRATA location. The fewest are available at the southwest extension sites and at 0°, 35°W, and the largest numbers are found along 23°W and at 20°N, 38°W. For each day in a PIRATA record with temperature available at a minimum of two levels, we first identify all missing levels, defined as depths of 1 m, and from 5 to 200 m in 5-m increments, that do not have PIRATA data on that day. For each missing depth, we obtain temperature at that depth from all Argo profiles in the ±90-day time span and the 2° × 3° region surrounding the mooring. We then obtain all Argo temperature data at the depths for which PIRATA temperature is available and perform multiple linear regression of the Argo temperatures at the available depths onto Argo temperatures at the missing depth. Using the resultant regression coefficients, we estimate the PIRATA temperature at the missing depth on the given day as

$$T_m = a_0 + \sum_{i=1}^{A} a_i T(z_i). \tag{1}$$

Here a_0 and a_i are the regression coefficients that convert PIRATA temperatures at the available depths $[T(z_i)]$ to temperature at the missing depth (T_m), and A is the number of depths for which PIRATA temperature is available on the given day. The Argo regression and (1) are repeated for each missing PIRATA depth on the given day, and then they are repeated for all days in a given PIRATA record. The result is a profile of temperature between 1 and 200 m at a 5-m vertical resolution on each day for which PIRATA temperature is available at a minimum of two depth levels. The same methodology is used for salinity, except Argo temperature and salinity profiles are used in the regression model because we found that the inclusion of temperature improves the model.

This method significantly reduces biases that result from simple linear interpolation between the nearest PIRATA depth levels and gives small reductions in RMS error relative to linear interpolation (Figs. 5, 6). For this comparison, we first retained Argo temperature data only at 20-m intervals between 20 and 140 m, and at 180 m; and salinity only at 20, 40, and 120 m. These are depths at which data are typically available at all moorings. The moorings also measure temperature and salinity at a depth of 1 m. Because Argo measurements are generally not available at 1 m, temperature and salinity at 10 m were used to represent values at a depth of 1 m. We then used 75% of the Argo data at each location to "train" the regression model and filled gaps in the remaining 25% of the profiles using the regression coefficients and the data at the available depths, based on (1). Note that in general these are not the exact errors associated with mapping the actual PIRATA data to a 5-m vertical grid, which depend on the depths at which PIRATA temperature is available on a given day, the specific mooring location and, to a lesser extent, the time of year. The calculation of these errors is described in the appendix.

Though the Argo regression method reduces biases introduced by the use of simple linear interpolation in depth, it occasionally generates unrealistic vertical gradients of temperature or salinity for cases in which the regression model has low predictability. To eliminate unrealistic temperature values, we first determine the maximum and minimum observed vertical temperature gradient over a distance of 5 m (i.e., between two vertical grid points), based on all Argo profiles within 2° of latitude and 3° of longitude of the mooring and for a given calendar month. If the vertical gradient for any ePIRATA daily-averaged profile, calculated between two depth levels, is outside of these upper and lower bounds set for each calendar month, the temperature at each depth level is removed and filled using the climatology (based on all data available at that depth) plus the anomaly vertically interpolated between the closest available depths with good data. However, if the original PIRATA data are available at a given depth, they are retained. The procedure is then repeated using gradients over a distance of 20 m. The same method is used to eliminate unrealistic salinity data. This results in the replacement of up to 5% of the temperature and salinity data at most locations.

When PIRATA temperature or salinity data are available at zero or one depth level, different techniques are used to fill the gaps. These gaps can occur, for example, if the mooring line breaks and the instruments are not recovered. If the temporal gap at a given level is 10 days or less, then linear interpolation in time is performed at that depth. If the gap is longer than 10 days,

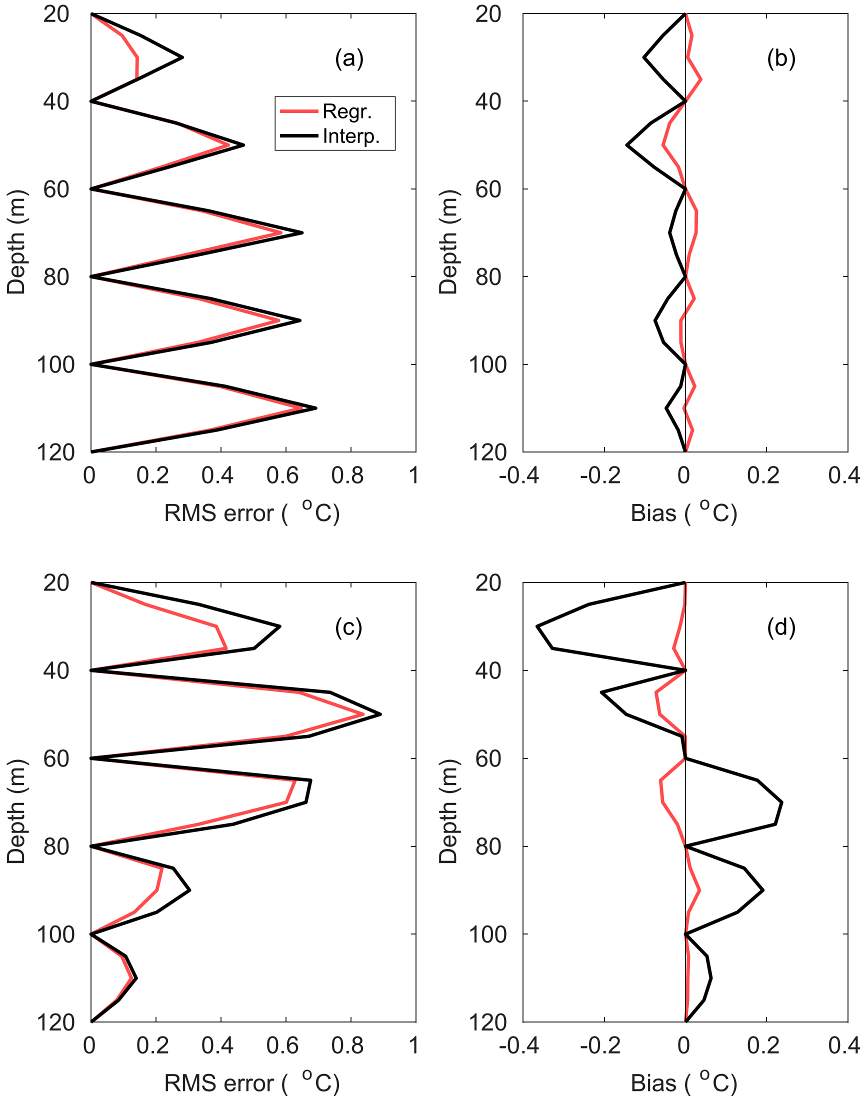

FIG. 5. (a) RMS difference between temperature from Argo profiles near the 4°N, 38°W mooring and temperature estimated using the Argo regression method (red) and linear interpolation between the two nearest depths (black). For the regression and interpolation methods, Argo profiles were subsampled every 20 m in depth. (b) As in (a), but with the mean bias between temperature estimated using the regression method (red) and linear interpolation (black). (c),(d) As in (a) and (b), respectively, but at the 0°, 10°W mooring location.

then optimum interpolation is performed, using all Argo profiles within ±10° of latitude, ±15° of longitude, and ±3 months from a given mooring on a given day. The cutoff of 10 days was chosen because we found that linear interpolation outperforms optimum interpolation at each location when the gap is less than about 10 days, and optimum interpolation is better for filling longer gaps. In practice, linear interpolation is rarely used, however, since less than 1% of the days at each location are part of a temperature or salinity gap that is 10 days or less. Optimum interpolation is more commonly performed, since as many as 44% of the days at some locations are part of gap that is longer than 10 days.

Following Reynolds and Smith (1994) and Kawai et al. (2006), optimum interpolation can be expressed as

$$A_k = F_k + \sum_{i=1}^{N} w_{k,i}(T_i - F_i). \qquad (2)$$

Here A_k is the interpolated "analysis" value for a given PIRATA location, day, and depth; F_k is the monthly climatological first-guess value from the

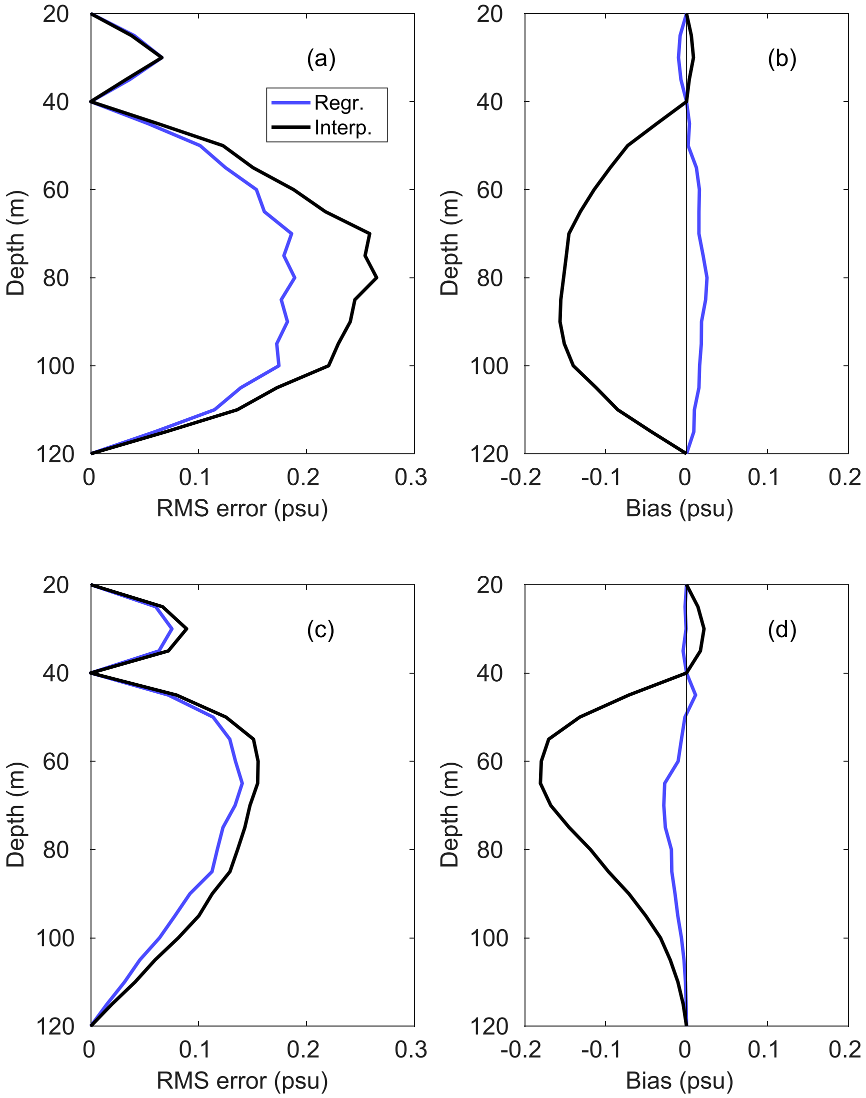

FIG. 6. As in Fig. 5, but for salinity. For the regression and interpolation methods, Argo profiles were subsampled at depths of 1, 20, 40, and 120 m.

World Ocean Atlas 2013 (*WOA13*; Locarnini et al. 2013; Zweng et al. 2013), linearly interpolated to the PIRATA location, calendar day, and depth; T_i and F_i are the individual Argo observations and the associated *WOA13* first-guess values, respectively, at location time i; and N is the total number of Argo profiles within the latitude, longitude, and time ranges specified previously. The weights [$w_{k,i}$ in (2)] can be expressed as

$$\Pi_{k,i} = \sum_{j=1}^{N} w_{k,j}\Pi_{ij}, \qquad (3)$$

where $\Pi_{k,i}$ is the correlation between the first-guess error at the mooring location and the error for a given Argo measurement, and Π_{ij} is the correlation between the first-guess errors associated with two given Argo measurements. We have assumed that the observational errors from individual Argo measurements are uncorrelated, and we use a Gaussian function in space and time for both sets of correlation coefficients, following Reynolds and Smith (1994):

$$\Pi_{ij} = \exp\left[-\left(\frac{x_i - x_j}{L_x}\right)^2 - \left(\frac{y_i - y_j}{L_y}\right)^2 - \left(\frac{t_i - t_j}{L_t}\right)^2\right]. \qquad (4)$$

Decorrelation scales are set to $L_x = 300\,\mathrm{km}$, $L_x = 200\,\mathrm{km}$, and $L_t = 15$ days, and the results are not very sensitive to other reasonable choices of these parameters. The percentage of depth levels filled with Argo optimal interpolation is up to 44% for salinity and up to 28% for temperature, depending on the gaps present in each PIRATA time series.

The resulting time series are then checked for static stability using the method of Jackett and McDougall (1995). If there is instability at a given depth, we determine whether it is caused by temperature, salinity, or both by performing the stability calculation again using constant salinity as a function of depth, and then using constant temperature. Unstable temperature and salinity values are replaced with the climatology plus the anomaly linearly interpolated between the closest depths with stable values. If there are still instabilities, the unstable values are replaced using linear interpolation in depth. Original PIRATA temperature and salinity data, with the exception of those removed using the methodology described earlier in this section, are retained regardless of the stability. Therefore, the result of the interpolation and stability checks is continuous daily time series of temperature and salinity at each PIRATA location, with 5-m vertical resolution, in which all original PIRATA data that pass quality control have been retained.

2) MLD AND SST GRADIENTS

The mixed layer depth (MLD) can be defined as the depth at which density is $\Delta\rho$ greater than the density at a depth of 1 m. Using the ePIRATA temperature and salinity, we choose a value of $\Delta\rho$ that is a balance between 1) maximizing the seasonal amplitude of MLD (periods > 180 days) relative to smaller time-scale variability (standard deviation of MLD high-pass filtered at a period = 10 days) and 2) minimizing the difference between SST and temperature averaged in the mixed layer (T). The reasoning behind this procedure is that it is desirable to have an MLD with a well-defined seasonal cycle that is not strongly influenced by spurious higher-frequency variations induced by uncertainties in the vertical interpolation of temperature and salinity. We choose a 10-day cutoff period for high-frequency variations so that intraseasonal variability is excluded, though the results are not very sensitive to the period chosen. Similar arguments were used by de Boyer Montégut et al. (2004), though they calculated MLD over the global ocean. In general, larger $\Delta\rho$ give stronger seasonal cycles of MLD and weaker high-frequency variations. The reason for requirement 2 is that it is advantageous for relating the terms in the mixed-layer heat and temperature budgets to changes in SST. For larger $\Delta\rho$ (increasing from 0 to 0.3 kg m^{-3}), the MLD, its seasonal amplitude, and the ratio of the seasonal amplitude to high-frequency variability all increase when averaged across all mooring locations (Fig. 7a). However, the difference between SST and T also increases, as does the seasonal amplitude of SST $-$ T (Fig. 7b). Based on these considerations, we define the MLD as the depth at which density is 0.12 kg m^{-3} greater than at 1 m. This definition results in a mean SST $-$ T of 0.06°C (black square in Fig. 7b) and a seasonal cycle of MLD that is 4 times larger than the amplitude of high-frequency variability (purple square in Fig. 7a). Our density criterion translates to a temperature criterion of about 0.35°C, which is similar to that chosen by de Boyer Montégut et al. (2004), considering that they used a reference depth of 10 m instead of our 1-m depth.

We use daily microwave SST to estimate horizontal mixed-layer temperature gradients, which are needed along with mixed layer depth and velocity to calculate horizontal temperature and heat advection—important terms in the mixed-layer temperature and heat budgets, respectively. The horizontal SST gradients are provided as part of the ePIRATA dataset. To determine the optimal spatial averaging to apply to the ¼° satellite SST data before computing gradients, we compared the RMS differences between daily satellite SST at each PIRATA location, using different spatial averaging, to daily SST from the mooring. We considered spatial averaging regions centered on the mooring location and ranging from 0.25° × 0.25° to 1.75° × 1.75°. The minimum RMS difference, averaged across all PIRATA locations, was found for a 1° × 1° average. The RMS difference tends to be larger for smaller averaging regions because of a smaller signal-to-noise ratio and increases for regions larger than 1° × 1° because the averaged SST is less representative of the mooring SST. We therefore use centered differences of 1° × 1° averages of satellite SST, calculated over a distance of 1°, to calculate horizontal SST gradients at each PIRATA location. For example, for zonal gradients at 0°, 35°W, SST is first averaged in 1° boxes centered at 35.5° and 34.5°W, then the difference between these spatial averages is calculated.

3) VELOCITY

At the off-equatorial locations with velocity measurements (see Table 1), we use the mooring data without correction and fill temporal gaps with a weekly surface drifter–altimetry–wind synthesis product (Lumpkin and Garzoli 2011) linearly interpolated to a daily time series at each mooring location. Daily anomalies from the seasonal cycle are added to the daily climatology calculated using all available PIRATA data at a given mooring. Comparisons between the mooring velocity time series and those from the drifter product and OSCAR revealed that the drifter product compares

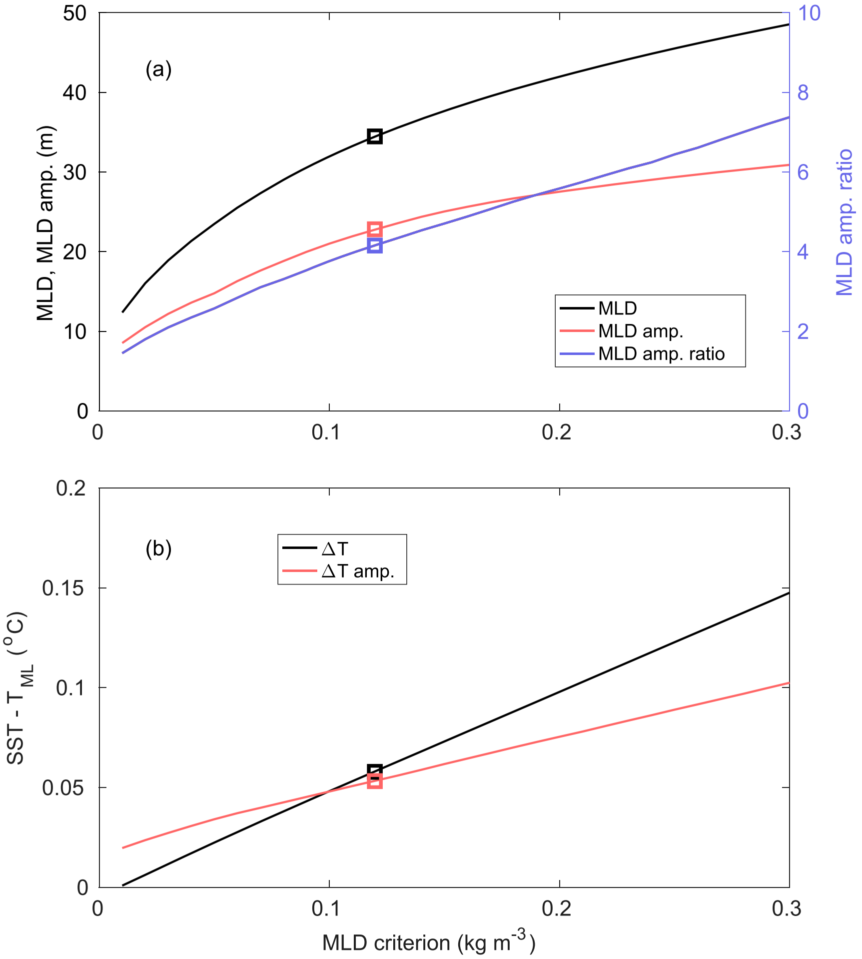

FIG. 7. (a) MLD (black), amplitude of the seasonal cycle of MLD (red), and ratio of the seasonal amplitude of MLD to the standard deviation of high-frequency (period < 10 days) MLD variability (purple) as a function of MLD criterion, based on an increase in density from the value at a depth of 1 m. Values have been averaged over all daily data and all PIRATA locations. (b) As in (a), but for the difference between SST and mixed-layer temperature (ΔT, black) and the amplitude of the seasonal cycle of ΔT (red). Both panels show the values corresponding to a MLD defined using a 0.12 kg m^{-3} criterion (squares).

more favorably at most locations in terms of annual mean and seasonal amplitude of zonal and meridional velocity. At 0°, 23°W we fill gaps with OSCAR, since the drifter product relies on Ekman balance for the wind-driven component and is therefore unavailable on the equator. At other equatorial locations, where no velocity data are available from the moorings, we also use OSCAR. The RMS differences and correlations between PIRATA 10-m velocity and the products used to fill gaps are shown in the appendix.

To convert the continuous records of 10-m velocity at each mooring location to vertically averaged velocity in the mixed layer (needed for the calculations of horizontal mixed-layer heat and temperature advection, and included in the ePIRATA dataset), we use monthly Ocean Reanalysis System 4 (ORAS4) data for 2000–14 (Balmaseda et al. 2013). In general, we found that ORAS4 velocity compares more favorably to PIRATA than the Simple Ocean Data Assimilation (SODA), the Global Ocean Data Assimilation System (GODAS), or the Estimating the Circulation and Climate of the Ocean (ECCO) products. This may be partly a result of the assimilation of PIRATA temperature and salinity measurements in ORAS4. For the zonal and meridional components separately, we regress the ORAS4 mixed-layer velocity onto the 10-m velocity and MLD. The multiple linear regression is performed at each PIRATA location, and the resulting coefficients are used along with daily MLD from the mooring location to adjust 10-m velocity to mixed-layer-averaged velocity. The result of

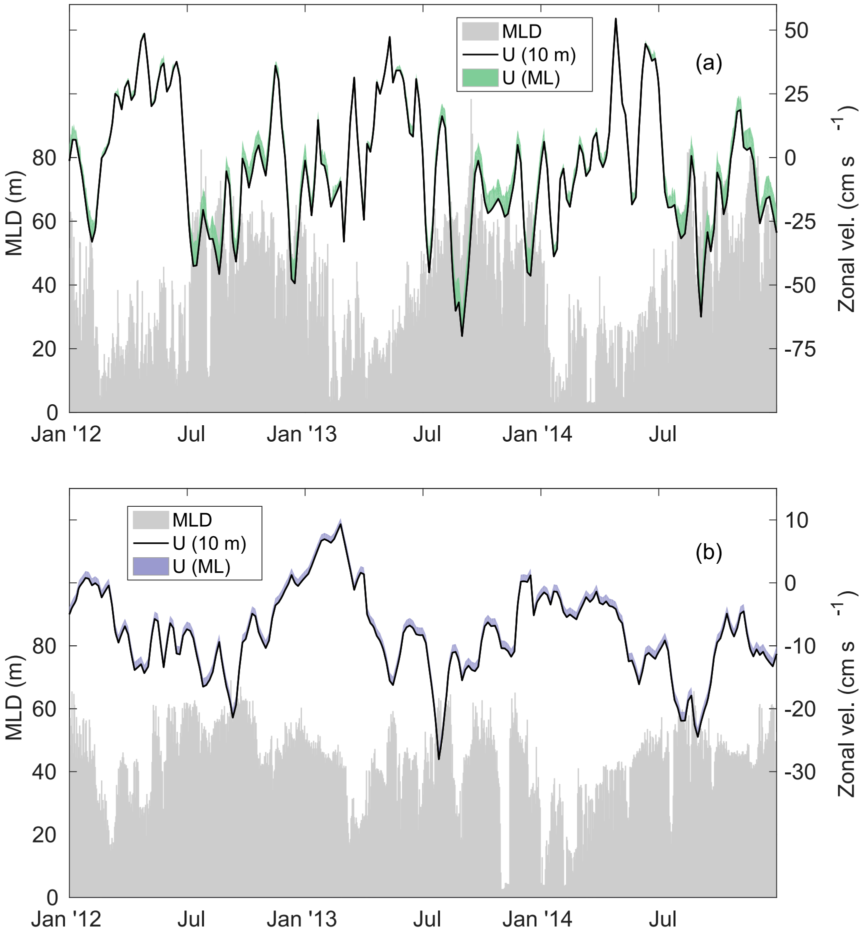

FIG. 8. (a) Time series of MLD (gray shading), zonal velocity at a depth of 10 m (black), and correction to 10-m velocity used to obtain the velocity vertically averaged in the mixed layer (green shading) at 0°, 35°W. (b) As in (a), but at 6°S, 10°W, and velocity correction (purple).

the correction is a mixed-layer velocity with a stronger eastward component at most locations. Record-length mean differences between mixed-layer and 10-m zonal velocity are -0.3 to $3.7\,\mathrm{cm\,s^{-1}}$ except at 0°, 23°W and 0°, 35°W, where the mean differences are 8.1 and $12.9\,\mathrm{cm\,s^{-1}}$ as a result of deep mixed layers and a strong Equatorial Undercurrent. There is a strong seasonality to the corrections along the equator, with the largest values during July–January, when the mixed layer is thickest (Fig. 8a). Mean corrections and seasonality are generally much weaker at the off-equatorial sites (Fig. 8b). Corrections to meridional velocity are -3.1 to $1.7\,\mathrm{cm\,s^{-1}}$ and are northward (>0) only at the Southern Hemisphere sites, reflecting the dominance of the poleward Ekman component, which is strongest at the surface.

c. *Mixed-layer heat and temperature budgets*

Mixed-layer heat and temperature budget analyses are useful techniques for assessing the causes of changes in mixed-layer heat content and SST, respectively. The heat budget equation can be expressed as

$$\rho c_p h \frac{\partial T}{\partial t} = -\rho c_p h \mathbf{v} \cdot \nabla T + Q_0 + Q_{-h}. \qquad (5)$$

Here h is the mixed layer depth; T is vertically averaged temperature in the mixed layer; $\mathbf{v}$ is horizontal velocity averaged in the mixed layer; ∇T is the horizontal gradient of T, estimated using satellite SST; Q_0 is the net surface heat flux, consisting of shortwave radiation absorbed in the mixed layer, net surface longwave radiation absorption, and latent and sensible heat fluxes; and Q_{-h} is the vertical turbulent flux of heat at the base of the mixed layer. The mixed-layer temperature equation is simply (5) divided by $\rho c_p h$. We use the ePIRATA daily time series to calculate each term in (5) and its temperature balance equivalent, with the exception of Q_{-h}, which can be estimated as the residual between the term on the left and the sum of the first two terms on the right. We have neglected a term in (5) that is proportional to the horizontal divergence of the vertically averaged temperature–velocity covariance [see Eq. (A19) of Moisan and Niiler 1998] because Foltz and McPhaden (2009) found that this term is insignificant in comparison to the other terms (annual means and monthly standard deviations are $<2\,\mathrm{W\,m^{-2}}$). Horizontal eddy heat advection on time scales less than one week is also not included in (5) because it cannot be calculated reliably using observations. This term may be important on the equator, where there are strong SST gradients and intraseasonal fluctuations of near-surface currents.

We estimate the shortwave radiation that penetrates the base of the mixed layer using an algorithm that depends on the surface chlorophyll-a concentration (chl-a), following Morel and Antoine (1994) and Sweeney et al. (2005) and using the 1998–2009 monthly mean seasonal cycle of chl-a from SeaWiFS. Algorithms that account for chl-a provide a significant improvement over those that rely on broader water-type classifications (Ohlmann 2003). An albedo of 6% (Payne 1972) is applied to the surface shortwave radiation before calculation of the penetrative component. The latent and sensible heat fluxes are calculated with version 3 of the Coupled Ocean–Atmosphere Response Experiment (COARE) bulk algorithm (Fairall et al. 2003) using the ePIRATA air temperature, relative humidity, wind speed, and SST time series. The ePIRATA mixed layer depth, mixed-layer temperature, horizontal mixed-layer velocity, and SST gradients are used to calculate heat storage rate and horizontal advection (first and second terms in the equation). Because the Q_{-h} term is difficult to calculate directly, we do not provide direct estimates of this term in our dataset.

Each term of the mixed-layer temperature budget is also provided in the dataset for more direct diagnosis of SST variability. The ePIRATA dataset contains daily-averaged values of each term in the heat and temperature budget equations at the 17 long-term PIRATA mooring locations, as well as daily time series of data used to calculate the budget terms, the depth of the 20°C isotherm, and the isothermal layer depth (useful for calculating barrier-layer thickness). Error estimates for these terms are also provided (see the appendix for details of their calculation). Figure 9 shows the period over which ePIRATA data are available at each location.

3. Results

Here we present examples of ePIRATA at selected locations and illustrate the usefulness of the time series for examining the processes responsible for changes in mixed-layer heat content and SST. Near-surface temperature from ePIRATA at 12°N, 38°W shows strong seasonal variations (Fig. 10a) tied to the meridional movement of the ITCZ and associated changes in wind speed and surface solar radiation (e.g., Foltz et al. 2003; Yu et al. 2006). The mixed layer depth and thermocline depth vary in phase (black and white lines in Fig. 10a, respectively), becoming shallowest in boreal summer and fall when the ITCZ is farthest north. Interannual variations of SST can be seen, most notably strong warm events in early 2005 and in 2010. Surface salinity also undergoes a strong seasonal cycle at 12°N, 38°W (Fig. 10b), decreasing abruptly in boreal fall and winter as low-salinity water from the ITCZ and Amazon River outflow is transported northward (e.g., Coles et al. 2013; Foltz et al. 2015). At 0°, 23°W the mixed layer and thermocline depths have weaker seasonal cycles compared to 12°N, 38°W (Figs. 10a,c). Near-surface salinity also undergoes weaker seasonal variability at 0°, 23°W, with the lowest values generally during boreal winter and spring (Fig. 10d), when SST and rainfall are highest and vertical mixing and

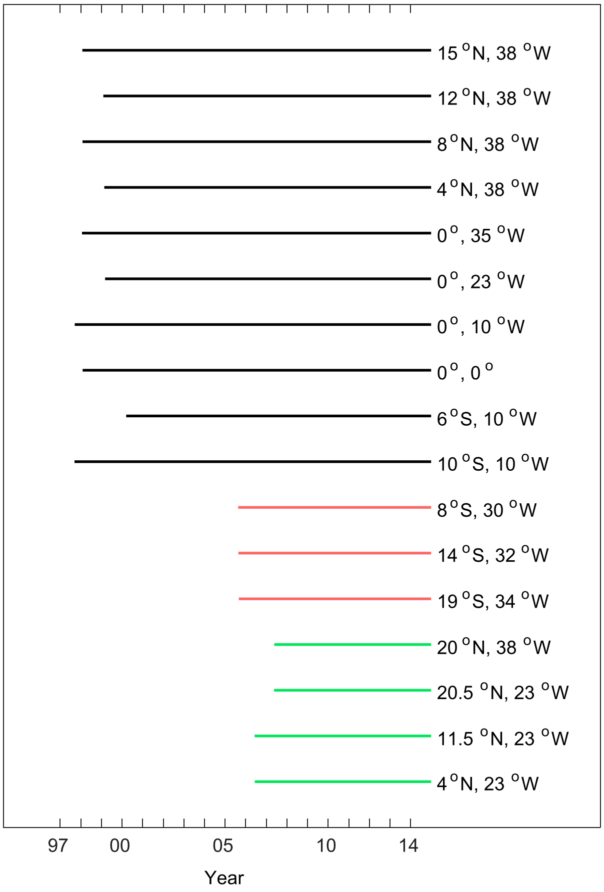

FIG. 9. Availability of daily ePIRATA data at each mooring location. Shown are "backbone" moorings (black), southwest extension (red), and northeast extension (green).

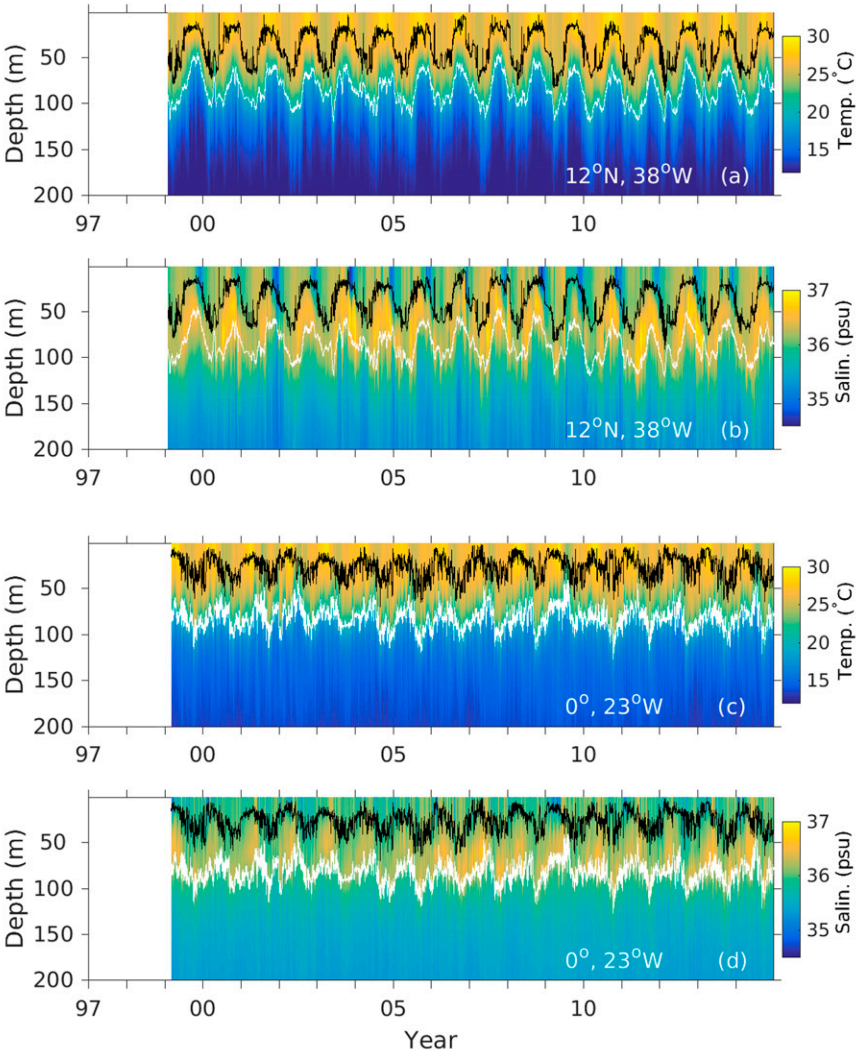

FIG. 10. The ePIRATA (a) temperature (color shaded), MLD (black line), and depth of the 20°C isotherm (white line) at 12°N, 38°W. (b) As in (a), except shading is salinity. (c),(d) As in (a) and (b), respectively, but at 0°, 10°W.

entrainment of saltier thermocline water are weakest (e.g., Da-Allada et al. 2013).

To illustrate the value of ePIRATA for heat budget studies, we show the daily mixed-layer heat storage rate, surface heat flux components, and horizontal mixed-layer heat advection at 0°, 23°W (Fig. 11). Changes in heat storage rate show strong short-time-scale variations (Fig. 11a) that are likely caused by lateral movements of the equatorial SST front. Error bars for the daily heat storage rate are generally less than 100 $\mathrm{W\,m^{-2}}$, but they become much larger when PIRATA data are unavailable and satellite SST or Argo data are used to fill the gaps (i.e., early 2005, middle of 2009, and late 2014). A full description of the errors is provided in the appendix. The amount of shortwave radiation absorbed in the mixed layer (Fig. 11b) shows a strong seasonal cycle. Error bars on this term are often less than 10 $\mathrm{W\,m^{-2}}$, but they increase to 20–40 $\mathrm{W\,m^{-2}}$ when gaps in the PIRATA record are filled with satellite data. There are strong seasonal and interannual variations of latent heat flux, and the error bars are consistently about 25 $\mathrm{W\,m^{-2}}$ (Fig. 11c). Finally, horizontal heat advection at 0°, 23°W (Fig. 11d) shows strong variability on daily to weekly time scales, peaking in boreal summer and fall, when the cold tongue is present and tropical instability wave (TIW) activity is strongest. In many years there is a secondary peak of variability in boreal winter, possibly related to the November–December central equatorial Atlantic zonal mode (Okumura and Xie 2006). Errors show a similar seasonality, reaching 150 $\mathrm{W\,m^{-2}}$

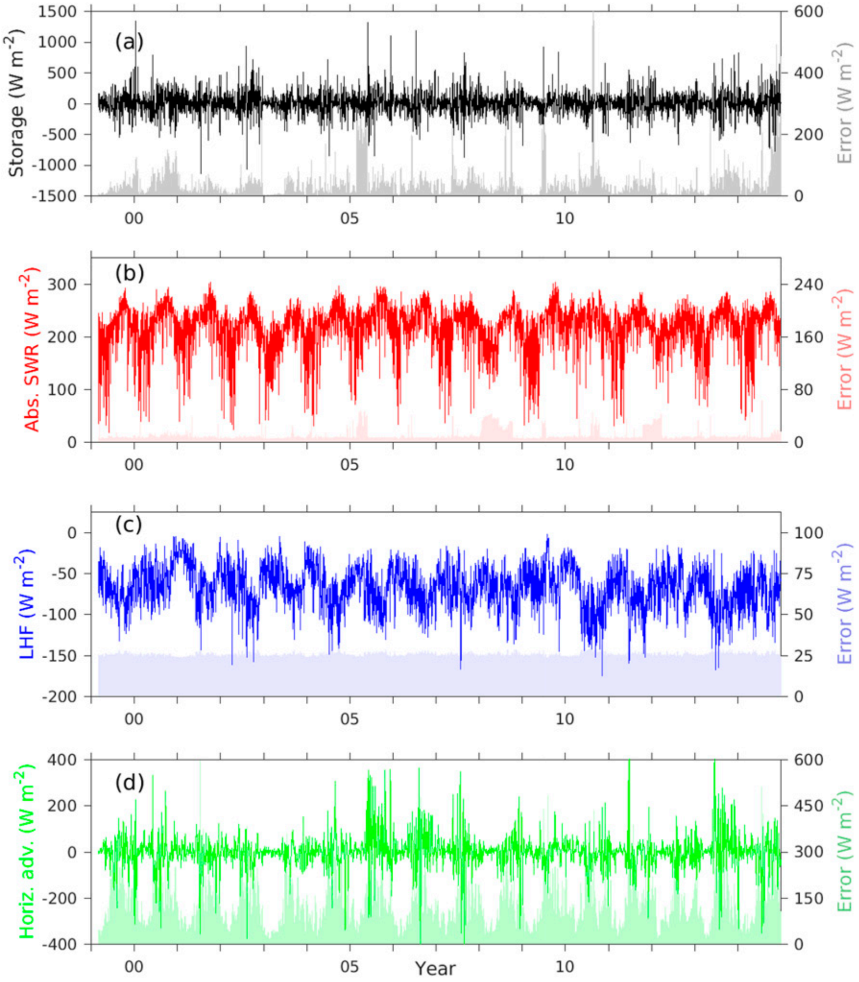

FIG. 11. The ePIRATA data at 0°, 23°W: (a) mixed-layer heat storage rate (black line), (b) SWR absorbed in the mixed layer (red line), (c) latent heat flux (blue line), and (d) horizontal mixed-layer heat advection (green line). In (a)–(d) shading indicates error estimates, with values on the right axis.

or higher in boreal summer and fall and dropping to about 50 W m^{-2} during the rest of the year. The large errors in summer, often exceeding the actual magnitude of horizontal advection, are caused by strong TIW velocities of up to 80 cm s^{-1}, combined with large uncertainties involved with estimating SST gradients with satellite data. Note that when averaged to monthly means, the errors are reduced by a factor of $3/(3)^{1/2}$, as discussed later in this section. For climatological monthly means, the errors are reduced by an additional factor of 2.8–4.1 because each ePIRATA time series is 8–17 yr long. Therefore, daily advection errors of 150 W m^{-2} are reduced to about 20 W m^{-2} for climatological monthly mean advection (Fig. 12). The heat budget terms show noticeable seasonal variations (Fig. 12) and seasonal modulations of interannual variability (vertical bars in Fig. 12), with the largest variances in heat storage rate and advection during boreal summer, when the cold tongue is developed, and the strongest interannual variations of shortwave radiation in boreal spring, when the ITCZ is near the equator.

One of the least frequently measured and least well-understood components of the mixed-layer heat budget is vertical turbulent mixing across the base of the mixed layer (Q_{-h}). This term can be estimated at each ePIRATA location as the difference between the mixed-layer heat storage rate and the sum of the net surface heat flux and horizontal advection. These estimates must be viewed with caution because of the accumulation of errors from other terms in the heat balance. However, a comparison of heat budget residuals to more direct measurements of the turbulent heat flux has shown good agreement (e.g., Moum et al. 2013; Hummels et al. 2014), indicating that the residual

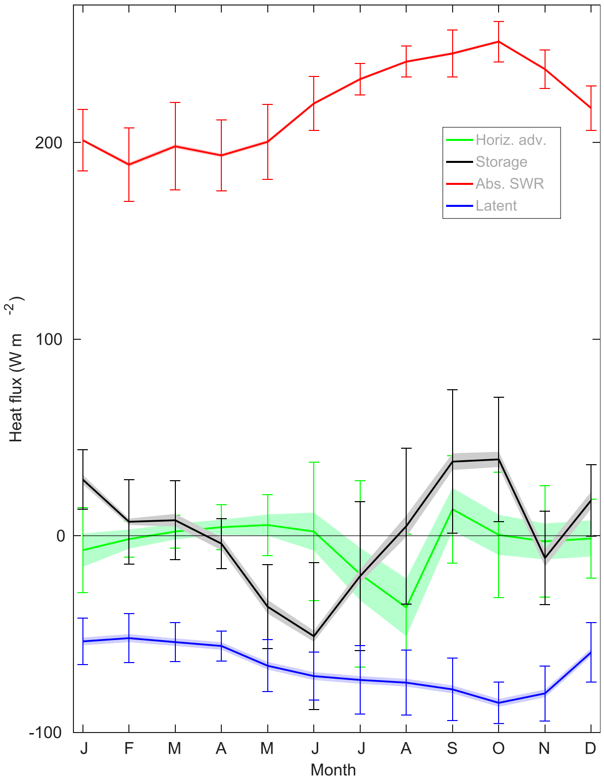

FIG. 12. The ePIRATA monthly mean climatological heat budget terms at 0°, 23°W: mixed-layer heat storage rate (black line), SWR absorbed in the mixed layer (red line), latent heat flux (blue line), and horizontal mixed-layer heat advection (green line). Shading indicates error estimates, and vertical error bars show the standard deviation for each calendar month across all years (a measure of interannual variability).

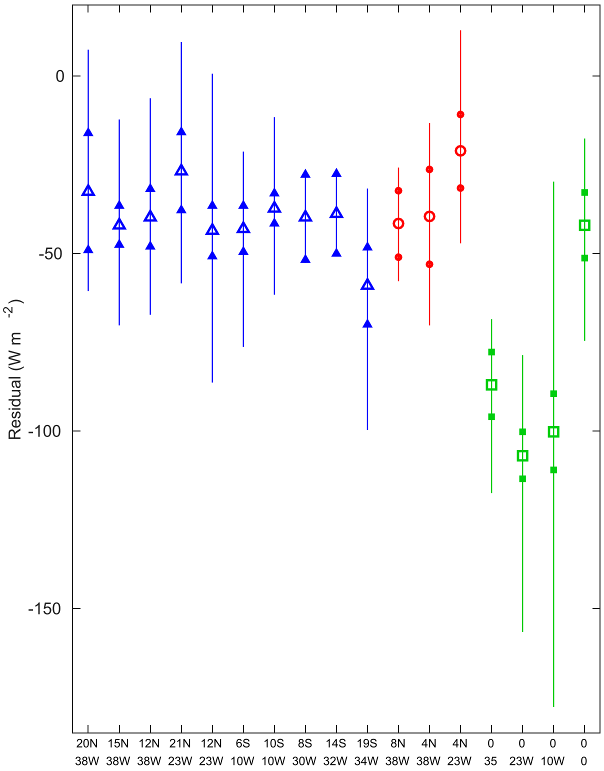

FIG. 13. Heat budget residual (heat storage rate − sum of net surface heat flux and horizontal advection) at each ePIRATA location. Shown are record-length mean (large symbols), range of climatological monthly values (lines), and error estimates for the annual mean (small symbols). Locations are indicated: outside of the ITCZ and equatorial regions (blue), in the ITCZ region (red), and on the equator (green).

can be used with some confidence to estimate vertical turbulent cooling. Estimates of vertical turbulent cooling based on parameterizations (e.g., Niiler and Kraus 1977; McPhaden 1982; Stevenson and Niiler 1983) are not provided in ePIRATA because of large uncertainties inherent in their calculations and in choosing the proper parameters and constants.

We first calculate the monthly mean seasonal cycle of each term in the heat budget from its daily time series and then compute record-length means. Errors are calculated using standard error propagation and then multiplied by $3/(3)^{1/2}$ to account for the ~3-day decorrelation time scale found for most variables. At all off-equatorial locations, the record-length mean Q_{-h} is between −60 and −20 W m^{-2} (Fig. 13; negative values indicate a tendency to cool the mixed layer). The smallest cooling from Q_{-h} occurs at 4°N, 23°W, which experiences weaker mean winds and higher surface solar radiation compared to many other sites because of its location close to the mean latitude of the ITCZ. Surprisingly, the other three locations in the ITCZ region, defined as an area in which climatological wind speed is less than 5 m s^{-1} for at least three months of the year (4°, 8°, and 12°N along 38°W; red symbols in Fig. 13), have a mean Q_{-h} that is similar to values at locations outside of the equatorial and ITCZ bands (blue symbols in Fig. 13). On the equator, there is significantly more cooling from Q_{-h} at 10°, 23°, and 35°W, with mean values of −110 to −85 W m^{-2} (green symbols in Fig. 13). In contrast, the mean Q_{-h} at 0°, 0° is comparable to that found at the off-equatorial sites. This reduction in cooling at 0°, 0° is believed to be caused by a decrease in vertical current shear (Jouanno et al. 2011; Hummels et al. 2014; Giordani and Caniaux 2014). It is unclear why Q_{-h} at 35°W is comparable to that at 10° and 23°W, since Jouanno et al. (2011) found a significant reduction in vertical turbulent cooling in the western equatorial Atlantic. Despite this difference, overall the results are consistent with previous studies, which show the strongest vertical turbulent cooling on the equator (e.g., Foltz et al. 2003; Peter et al. 2006; Hummels et al. 2013). The ePIRATA estimates of Q_{-h} show strong seasonal variations at many locations, and the largest peak-to-peak amplitude of 150 W m^{-2} occurs at 0°, 10°W (vertical lines in Fig. 13).

To explore the possible causes of seasonal variations of Q_{-h}, we first calculate its seasonal range, $Q_{-h}(\Delta S) = Q_{-h}(S_{\max}) - Q_{-h}(S_{\min})$, where $S_{\max}$ is the 3-month season [December–February (DJF), January–March (JFM), February–April (FMA), etc.] with the largest mean cooling from Q_{-h} (i.e., most negative value) and $S_{\min}$ is the 3-month season with the smallest mean cooling from Q_{-h}. We then calculate the difference in wind speed between these seasons, $W(\Delta S) = W(S_{\max}) - W(S_{\min})$, since wind speed is known to affect the rate of vertical turbulent mixing. We also calculate the difference in the standard deviation of the diurnal cycle of SST, $D(\Delta S) = D(S_{\max}) - S(S_{\min})$, using 10-min averages of temperature at a depth of 1 m from the PIRATA moorings. The standard deviation is first calculated for each calendar month using all available 10-min measurements, after applying a 36-h high-pass filter. Term $D(\Delta S)$ is then calculated from the monthly values. Studies of turbulent mixing on the equator have indicated that the diurnal cycle is important (e.g., Moum et al. 2011), and here we explore whether the same may be true at off-equatorial locations in the Atlantic. The diurnal cycle of SST is used as a proxy for diurnal variations of mixed layer depth and current shear, since previous studies have shown strong relationships between these parameters (e.g., Cronin and Kessler 2009).

Comparison of $Q_{-h}(\Delta S)$ and $W(\Delta S)$ shows that at 15 of 17 locations, winds are weaker [$W(\Delta S)$ negative] during the season with the strongest Q_{-h} cooling than during the season with the weakest cooling (Fig. 14a). For large negative values of $W(\Delta S)$ (<1 m s^{-1}), there is a tendency for larger values of $Q_{-h}(\Delta S)$ to be associated with larger values of $W(\Delta S)$. At most of these locations, the seasonal range of wind speed is close to $W(\Delta S)$ (not shown), suggesting that stronger seasonal variations of wind speed may drive stronger seasonal cycles of Q_{-h}. At off-equatorial locations, the correlation between $Q_{-h}(\Delta S)$ and $W(\Delta S)$ is 0.53 across all locations (winds are weaker when cooling is stronger), and this correlation is significant at the 90% level. Along the equator, the relationship between $Q_{-h}(\Delta S)$ and $W(\Delta S)$ is very weak, likely because of the importance of seasonal variations in current shear driven by the equatorial undercurrent (Jouanno et al. 2011; Hummels et al. 2014).

The tendency for cooling from Q_{-h} to be strongest when wind speed is weakest may be related to the tendency for a thinner mixed layer and stronger diurnal cycle when winds are weak (Fairall et al. 1996a). At 11 of 13 off-equatorial locations, the mixed layer is thinner in the season with the strongest Q_{-h} cooling than in the season with the weakest Q_{-h} cooling (not shown). We also found that the diurnal cycle of SST tends to be stronger in the season with the strongest Q_{-h} cooling [$D(\Delta S) > 0$ in Fig. 14b]. At off-equatorial locations, the correlation between $Q_{-h}(\Delta S)$ and $D(\Delta S)$ is -0.64 (diurnal cycle is stronger when cooling is stronger), significant at the 95% level. The correlation drops to -0.43 when equatorial sites are included.

Previous studies have shown the importance of the diurnal cycle for generating vertical current shear and vertical turbulent mixing in the equatorial Pacific (Cronin and Kessler 2009; Moum et al. 2011; Smyth et al. 2013; Pham et al. 2013) and Atlantic (Wenegrat and McPhaden 2015). Stronger and shallower stratification during daytime is associated with stronger near-surface currents and vertical shear, which descends and generates enhanced turbulent mixing as surface solar heating decreases. On the equator, the equatorial undercurrent provides an essential source of vertical current shear, explaining the large annual mean turbulent cooling on the equator (Fig. 13; Jouanno et al. 2011; Hummels et al. 2014). We hypothesize that even at off-equatorial locations there may be enough diurnally driven current shear below the mixed layer and mixed-layer deepening (i.e., entrainment mixing) to generate significant turbulent cooling of the mixed layer. Despite weaker winds when the diurnal cycle is most active, the thinner mixed layer and stronger stratification may lead to stronger near-surface current shear than during periods without a strong diurnal cycle, thus possibly explaining the tendency for Q_{-h} to be largest when winds are weakest and the diurnal cycle is strongest (Fig. 14).

The importance of the diurnal cycle may also explain why at off-equatorial locations the annual mean Q_{-h} values are similar, even with an annual mean wind speed varying between 4.5 and 7 m s^{-1}. At locations with stronger mean winds, the mixed layer tends to be thicker (the correlation between annual mean wind speed and mixed layer depth is 0.4 across all off-equatorial locations) and the diurnal SST standard deviation tends to be smaller (a correlation of -0.8 between annual mean wind speed and diurnal SST standard deviation). Stronger winds by themselves tend to generate more mixing, but at the base of the mixed layer this increase may be balanced by a decrease in mixing because of an increase in mixed layer depth, acting to reduce current shear, and a decrease in diurnal cycle amplitude and associated entrainment cooling. These hypotheses will need to be tested using numerical models and direct measurements of current shear and turbulent mixing.

4. Summary

A new daily enhanced PIRATA (ePIRATA) dataset has been developed that fills temporal gaps and maps

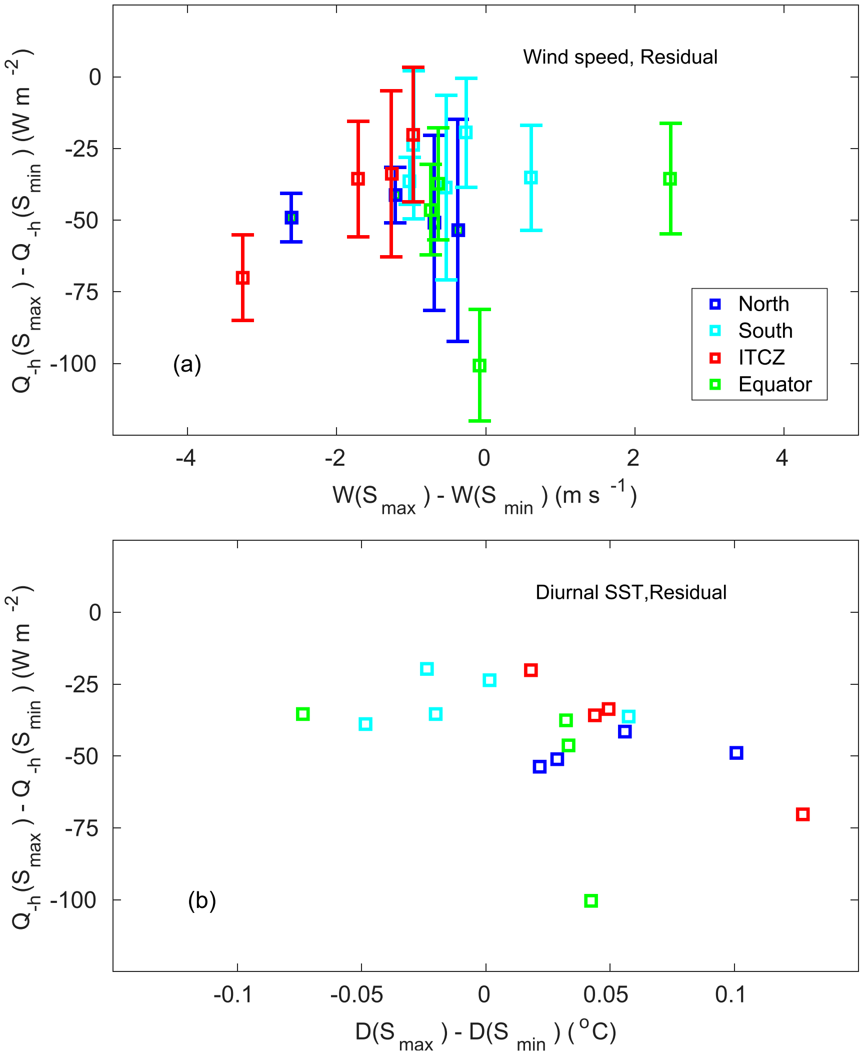

FIG. 14. Scatterplots of the seasonal range of Q_{-h} at each ePIRATA location, calculated as the difference between the 3-month season (S_{max}) with the largest mean cooling from Q_{-h} (i.e., most negative value) and the 3-month season (S_{min}) with the smallest cooling, vs (a) the corresponding wind speed difference, $W(S_{max}) - W(S_{min})$, and (b) the difference in the diurnal amplitude of SST. Locations in the Northern Hemisphere (dark blue) and Southern Hemisphere (light blue), and outside of the ITCZ; within the ITCZ (red); and on the equator (green). Bars in (a) represent error estimates for each seasonal difference of Q_{-h}. Error bars for wind speed in (a) and SST in (b) are <0.1 m s^{-1} and 0.01°C, respectively, and are not shown.

subsurface temperature and salinity to depths of 1 m and with 5-m vertical spacing between 5 and 200 m. All original PIRATA data are retained after elimination of questionable data, and detailed error estimates are provided. The resultant continuous daily time series at each of the 17 PIRATA locations are then used to calculate the terms in the mixed-layer heat and temperature budgets and their error bars. This dataset complements the tropical Atlantic portions of global datasets, such as OAFlux, TropFlux, and OSCAR, which use PIRATA measurements only for validation or to correct for biases. In contrast, ePIRATA consists of the highest-quality basin-scale, collocated time series of upper-ocean and near-surface atmospheric measurements, which we anticipate will be valuable for studies of the upper ocean and air–sea heat and moisture exchange. ePIRATA is available online (http://www.aoml.noaa.gov/phod/epirata/) and will be updated in the middle of each year to extend through the end of the previous year.

As an example of the application of ePIRATA, the vertical turbulent exchange of heat across the base of the mixed layer was estimated as the difference between the mixed-layer heat storage rate and the sum of the net surface heat flux and horizontal advection at each ePIRATA location. On average, vertical mixing acts to reduce the mixed-layer heat content at off-equatorial locations and 0°, 0° by 20–60 $\mathrm{W\,m^{-2}}$. On the equator at 10°, 23°, and 35°, mean rates of heat content reduction are 85–110 $\mathrm{W\,m^{-2}}$. Significant seasonal variations of vertical turbulent cooling are found at most locations, and the largest peak-to-peak amplitude of 150 $\mathrm{W\,m^{-2}}$ was found at 0°, 10°W. Off the equator, the seasonal maximum of turbulent cooling tends to occur when winds are weak and the diurnal variability of SST is strong. These results suggest that the interplay between the diurnal cycle, stratification, and current shear may be important for explaining off-equatorial vertical turbulent cooling of the mixed layer.

In addition to its value for upper-ocean and climate research and model validation, ePIRATA presents a framework for assessing the value of additional PIRATA sensors for reducing uncertainties in upper-ocean temperature and salinity, mixed layer depth and currents, and mixed-layer heat and temperature budget components. It is anticipated that the largest potential to reduce uncertainties in mixed layer depth and currents is through the addition of one or two current meters in the mixed layer at each mooring location and additional salinity sensors in the upper 50–100 m.

Acknowledgments. Support was provided by the Ocean Observing and Monitoring Division of NOAA's Climate Program Office and by base funds to NOAA's Atlantic Oceanographic and Meteorological Laboratory. We are grateful to the U.S., French, and Brazilian PIRATA teams and the TAO Project Office for maintaining the array and for providing data free to the public. Argo data were obtained from a Global Data Assembly Centre (Argo GDAC, doi:10.17882/42182). We thank three anonymous reviewers, whose helpful comments improved the quality of the manuscript.

APPENDIX

Data Availability and Error Estimates

In this appendix we briefly summarize the availability of data at each PIRATA location and the agreement between PIRATA measurements and the reconstructed data used to fill gaps. We then describe the methodology used to calculate error bars for each of the daily ePIRATA parameters described in the main text. These errors are included in the ePIRATA dataset along with the corresponding daily time series of each parameter.

TABLE A1. Percentage of daily data that is missing at each PIRATA location. Columns show values for air temperature (AT), relative humidity (RH), wind speed (WS), shortwave radiation (SWR), longwave radiation (LWR), ocean temperature (Temp), salinity (Salin), and velocity at a depth of 10 m (Vel).

	AT	RH	WS	SWR	LWR	Temp	Salin	Vel
20°N, 38°W	14	14	20	25	72	26	36	51
15°N, 38°W	4	5	14	3	21	11	31	41
12°N, 38°W	5	8	17	2		12	32	
8°N, 38°W	14	11	30	9		11	44	
4°N, 38°W	12	10	25	16		20	34	
20.5°N, 23°W	1	9	13	1		10	24	50
11.5°N, 23°W	18	19	16	14	17	15	15	36
4°N, 23°W	1	1	6	19		10	29	41
0°, 35°W	10	7	16	10		14	50	
0°, 23°W	6	6	26	9	16	16	26	58
0°, 10°W	29	38	47	27		33	37	
0°, 0°	30	32	41	34		31	41	
6°S, 10°W	1	1	18	7		10	32	
10°S, 10°W	5	5	10	25	13	9	21	46
8°S, 30°W	9	9	9	9		16	23	
14°S, 32°W	6	6	7	10		10	14	
19°S, 34°W	15	15	9	5	1	10	26	

Also included in the dataset are flags indicating the quality of the data that went into the calculation of each parameter. A flag of "0" indicates that some or all of the data that went into the calculation of that parameter came from sources other than PIRATA (e.g., a value of 0 is assigned for temperature at a depth of 50 m if a direct measurement from a PIRATA sensor is not available on that day at that depth). A flag of 1 indicates that original PIRATA data were used, and a flag of 2 means that original PIRATA data were used but that a bias correction was applied (applicable for shortwave data at several locations between 8° and 20.5°N).

a. *PIRATA data availability and quality of reconstructed data*

Table A1 shows the percentage of days with missing data for each variable at each location. For this calculation, we take into account only the period after the start of the time series for a given variable at a given location. For this reason, there are blanks in Table A1 if a parameter has never been measured. For subsurface temperature and salinity, all depth levels are used in the calculation. The availability of PIRATA data varies across locations and variables (Table A1). In general, there are more missing subsurface temperature, salinity, and velocity data than meteorological data. At many locations, more than 25% of the data are missing for at least one variable, and in some cases 40% or more of salinity or velocity is missing. Note that the high percentage of missing longwave radiation data at 20°N, 38°W results from measurements made for only about

Table A2. Comparisons between daily PIRATA measurements and data used to fill gaps. Shown are the RMS differences and correlations (parentheses) at each location for air temperature (AT), relative humidity (RH), wind speed (WS), shortwave radiation (SWR), and longwave radiation (LWR). Calculations at each location are based only on periods when PIRATA and gap-filling data are available.

	AT	RH	WS	SWR	LWR
20°N, 38°W	0.1 (0.99)	2.1 (0.93)	0.5 (0.97)	20.9 (0.92)	
15°N, 38°W	0.2 (0.99)	3.4 (0.81)	0.5 (0.96)	35.7 (0.73)	6.0 (0.93)
12°N, 38°W	0.3 (0.98)	3.2 (0.76)	0.7 (0.95)	37.6 (0.71)	
8°N, 38°W	0.3 (0.91)	3.0 (0.75)	0.6 (0.96)	42.3 (0.72)	
4°N, 38°W	0.3 (0.90)	2.8 (0.81)	0.6 (0.94)	40.0 (0.78)	
20.5°N, 23°W	0.2 (0.99)	2.2 (0.94)	0.5 (0.97)	24.0 (0.88)	
11.5°N, 23°W	0.2 (0.99)	2.2 (0.88)	0.4 (0.98)	26.4 (0.82)	
4°N, 23°W	0.2 (0.95)	2.4 (0.87)	0.6 (0.95)	32.1 (0.79)	
0°, 35°W	0.3 (0.89)	2.5 (0.78)	0.5 (0.96)	34.0 (0.77)	
0°, 23°W	0.3 (0.96)	3.1 (0.60)	0.5 (0.96)	29.2 (0.70)	4.7 (0.94)
0°, 10°W	0.3 (0.99)	2.4 (0.84)	0.5 (0.93)	28.3 (0.68)	
0°, 0°	0.5 (0.96)	2.5 (0.76)	0.5 (0.93)	32.3 (0.70)	
6°S, 10°W	0.3 (0.99)	3.0 (0.73)	0.4 (0.94)	31.0 (0.67)	
10°S, 10°W	0.3 (0.98)	3.5 (0.66)	0.5 (0.93)	31.2 (0.80)	7.1 (0.79)
8°S, 30°W	0.2 (0.98)	2.0 (0.86)	0.4 (0.96)	20.5 (0.89)	
14°S, 32°W	0.1 (0.99)	2.1 (0.85)	0.4 (0.96)	21.1 (0.91)	
19°S, 34°W	0.2 (0.99)	2.6 (0.90)	0.6 (0.96)	26.7 (0.91)	4.6 (0.95)

2 months in 2011 and 10 months in 2013, after which the longwave radiation sensor was not redeployed.

Table A2 shows the agreement between daily mean PIRATA measurements and the data used to fill gaps in the PIRATA meteorological records. The RMS differences and correlations are calculated using days when both the PIRATA measurements and gap-filling data are available. Correlations are generally highest for air temperature and wind speed (0.89–0.99) and lower for relative humidity and radiation (0.60–0.94). The agreement is good for SST, with correlations of at least 0.8, but worse for sea surface salinity (SSS) and 10-m ocean velocity, with correlations generally between 0.4 and 0.8 (Table A3). The near-zero correlation for SSS at 19°S, 34°W is due to a very weak seasonal cycle of SSS, resulting in a very low signal-to-noise ratio for the satellite SSS used to fill gaps.

b. *Ocean temperature and salinity errors*

Errors in subsurface temperature and salinity result primarily from 1) vertical interpolation between PIRATA depth levels, 2) filling of temporal gaps in PIRATA records with Argo optimum interpolation, and 3) PIRATA instrumental uncertainties. Errors from cases 1 and 3 are applicable only when PIRATA data at more than one depth are available on a given day (otherwise, Argo optimum interpolation is used and the mooring data are not), and case 2 is relevant only when PIRATA data are available at zero or one depth. For case 1, all Argo profiles within ±2° of latitude and ±3° of longitude from a given mooring, and within ±30 days of a given mooring day (regardless of the year in which the Argo data reside) are obtained. These profiles are then used to calculate the RMS difference between the interpolated temperature or salinity at each missing level, based on the regression method described in section 2b(1), and the actual Argo temperature or salinity at that level. For PIRATA days on which temperature or salinity at a depth of 1 m has been filled with either satellite SST or SSS, the uncertainty at that level is instead estimated as the RMS difference between

Table A3. As in Table A2, but for values for SST, SSS, and zonal and meridional velocity at a depth of 10 m (U and V, respectively).

	SST	SSS	U	V
20°N, 38°W	0.3 (0.98)	0.1 (0.38)	8.1 (0.72)	8.7 (0.69)
15°N, 38°W	0.3 (0.98)	0.2 (0.55)	7.8 (0.45)	8.1 (0.40)
12°N, 38°W	0.4 (0.96)	0.2 (0.59)		
8°N, 38°W	0.4 (0.92)	0.4 (0.82)		
4°N, 38°W	0.3 (0.80)	0.2 (0.69)		
20.5°N, 23°W	0.3 (0.99)	0.2 (0.56)	8.1 (0.63)	6.5 (0.72)
11.5°N, 23°W	0.4 (0.98)	0.2 (0.76)	12.3 (0.46)	11.3 (0.50)
4°N, 23°W	0.4 (0.87)	0.3 (0.63)	16.4 (0.56)	18.1 (0.53)
0°, 35°W	0.3 (0.88)	0.2 (0.65)		
0°, 23°W	0.4 (0.96)	0.2 (0.78)	25.5 (0.50)	19.4 (0.40)
0°, 10°W	0.4 (0.98)	0.4 (0.81)		
0°, 0°	0.5 (0.96)	0.3 (0.88)		
6°S, 10°W	0.3 (0.99)	0.1 (0.78)		
10°S, 10°W	0.3 (0.98)	0.1 (0.79)	6.6 (0.52)	6.6 (0.48)
8°S, 30°W	0.2 (0.97)	0.1 (0.63)		
14°S, 32°W	0.3 (0.97)	0.2 (0.67)		
19°S, 34°W	0.3 (0.98)	0.1 (0.06)		

PIRATA and satellite SST or SSS for that climatological day. The result is an uncertainty estimate, consisting of one of the aforementioned RMS differences, for each day on which PIRATA measurements at a minimum of two depth levels are available.

To calculate uncertainties for case 2, in which PIRATA measurements are available at fewer than two depths on a given day, we perform optimum interpolation at each Argo profile location within ±10° of latitude and ±15° of longitude of the mooring, using all other Argo profiles that are within ±10° of latitude and ±15° of longitude and ±3 months of the profile location and following the methodology used for the Argo optimum interpolation at the PIRATA locations described in section 2b(1). The interpolation is performed at each ePIRATA depth level separately. At each depth, the RMS difference between the optimally interpolated value and the actual Argo value is calculated and the monthly climatology of the RMS difference is fit to an annual harmonic. For a given ePIRATA day and depth, the uncertainty in temperature or salinity is obtained from the corresponding monthly annual cycle of RMS difference.

When PIRATA measurements are available at more than one depth on a given day, instrumental uncertainties of ±0.003°C and ±0.02 psu are used for temperature and salinity, respectively (www.pmel.noaa.gov/tao/proj_over/sensors.shtml), at the ePIRATA depths corresponding to those measurements. The temperature error at each depth and on each day (ϵ_T) is calculated from either case 1, case 2, or case 3, and similarly for the salinity error (ϵ_S). When vertical interpolation is used between PIRATA temperature values, errors are typically 0°–0.5°C at off-equatorial locations, increasing to 0°–1°C in the eastern equatorial Atlantic. Temperature errors are as high as 2°C on days when all PIRATA data are missing. Salinity errors are 0–0.15 psu when vertical interpolation is used, and up to 0.3 psu when all PIRATA data are missing.

c. MLD, velocity, and SST gradient errors

We use ePIRATA temperature, salinity, ϵ_T, and ϵ_S to calculate errors in mixed layer depth (MLD). First, for a given day, a random value of the temperature error at each depth is obtained using a normal distribution with a standard deviation set to ϵ_T, and similarly for the salinity error. These random temperature and salinity errors are then added to the ePIRATA temperature and salinity profiles, respectively, for that day. If there is static instability in the resultant density profile, then the random error generation is repeated until there is stability or the number of iterations reaches 50, whichever occurs first. The MLD is then calculated from the resultant temperature and salinity profiles. All of the above-mentioned steps are performed 10 times, giving 10 different MLD values for a given PIRATA day. The standard deviation of these values is then used as the uncertainty estimate for MLD. Typical errors for daily-averaged MLD are 3–10 m, with the smallest values along the equator, where mean MLDs are smallest. Relative errors (record-length mean daily error divided by record-length mean MLD) are about 10%–25%. The procedure for estimating MLD errors is repeated to calculate errors for the isothermal layer depth, the depth of the 20°C isotherm, and the vertically averaged temperature in the mixed layer.

To calculate errors in the mixed-layer velocity estimates, we consider three main sources of uncertainty: 1) use of the drifter–altimetry product to fill gaps in the PIRATA records, 2) converting from 10-m velocity to velocity averaged in the mixed layer, and 3) PIRATA instrumental uncertainty, when direct measurements from current meters are available. At locations with some PIRATA velocity measurements (Table 1), the daily RMS difference between the PIRATA values and the drifter–altimetry values ($\epsilon V_{\mathrm{fill}}$) are used for source 1. At locations with no direct measurements, we use the errors from nearby locations with measurements: 4°N, 23°W errors are used at 4°N, 38°W and 8°N, 38°W; 15°N, 38°W errors are used at 12°N, 38°W; 0°, 23°W errors are used at all equatorial locations; and 10°S, 10°W errors are used at all locations in the South Atlantic. For errors associated with converting 10-m velocity to mixed-layer velocity (error 2), we use the RMS difference between the mixed-layer velocity from monthly ORAS4 data (1958–2014) and the mixed-layer velocity predicted by the multiple linear regression described in section 2b(2) (ϵV_{dz}). A constant value of $\pm 5\,\mathrm{cm\,s^{-1}}$ is used for all instrumental errors ($\epsilon V_{\mathrm{instr}}$) (www.pmel.noaa.gov/tao/proj_over/sensors.shtml). The total uncertainty in mixed-layer velocity (zonal or meridional) at a given location for a given ePIRATA day is $\epsilon_V = \sqrt{\epsilon V_{\mathrm{fill}}^2 + \epsilon V_{\mathrm{dz}}^2 + \epsilon V_{\mathrm{instr}}^2}$ for days with no PIRATA data at locations with some PIRATA data on other days ($\epsilon V_{\mathrm{instr}}$ is included in this case because the PIRATA seasonal cycle is added to anomalies of drifter–altimetry or OSCAR velocity), $\epsilon_V = \sqrt{\epsilon V_{\mathrm{fill}}^2 + \epsilon V_{\mathrm{dz}}^2}$ for locations with no PIRATA velocity data, and $\epsilon_V = \sqrt{\epsilon V_{\mathrm{dz}}^2 + \epsilon V_{\mathrm{instr}}^2}$ for days with PIRATA data. Daily velocity errors range from 5 to $30\,\mathrm{cm\,s^{-1}}$ within 4° of the equator and decrease to $5–10\,\mathrm{cm\,s^{-1}}$ poleward of 4°N.

To calculate errors in horizontal gradients of SST ϵ_{SST}, first, the RMS difference between daily satellite SST and daily PIRATA temperature at a depth of 1 m is calculated for each calendar month using data from all years. Errors in the zonal gradient of SST are calculated as

$\epsilon_{\mathrm{dx}} = \sqrt{2\epsilon_{\mathrm{SST}}^2}/\Delta x$. Here Δx is the 1° distance (m) centered on each PIRATA location. Errors in the meridional gradients of SST are calculated similarly. Errors in horizontal heat advection are calculated from the errors in MLD, velocity, and SST gradients using standard error propagation and assuming that the errors in each term are uncorrelated.

d. Atmospheric data errors

There are four main sources of error in ePIRATA surface shortwave radiation (SWR). 1) Uncertainties associated with estimating SWR from satellite OLR are calculated at each location as the RMS difference between daily PIRATA SWR and OLR-based SWR within a given calendar month, using data from all years ($\epsilon\mathrm{SWR}_{\mathrm{OLR}}$). 2) The uncertainty in using the clear-sky method to correct PIRATA SWR for biases caused by dust buildup is calculated as the standard deviation of the daily clear-sky bias at 14°S, 32°W, where the dust-induced bias is very close to zero ($\epsilon\mathrm{SWR}_{\mathrm{CS}}$). This gives a single number ($7\,\mathrm{W\,m^{-2}}$) that is used across all locations and for all days. 3) Errors caused by short-duration (less than about one month) dust deposition events that are not fully accounted for in the clear-sky correction technique are estimated to be 20% of the SWR correction applied on a given day ($\epsilon\mathrm{SWR}_{\mathrm{ST}}$). 4) An instrumental error of ±2% is used for the PIRATA solar radiometers ($\epsilon\mathrm{SWR}_{\mathrm{instr}}$). On days for which PIRATA SWR is not available and OLR-based SWR is used instead, the total error is calculated as $\epsilon_{\mathrm{SWR}} = \sqrt{\epsilon\mathrm{SWR}_{\mathrm{instr}}^2 + \epsilon\mathrm{SWR}_{\mathrm{OLR}}^2}$. Note that instrumental errors are included here because the OLR-based SWR anomalies are added to the mean seasonal cycle of mooring SWR, and similarly for other atmospheric time series described later in this section. On days with direct PIRATA measurements for which a dust correction was applied, the error is $\epsilon_{\mathrm{SWR}} = \sqrt{\epsilon\mathrm{SWR}_{\mathrm{instr}}^2 + \epsilon\mathrm{SWR}_{\mathrm{CS}}^2 + \epsilon\mathrm{SWR}_{\mathrm{ST}}^2}$. On days with PIRATA measurements and no dust correction, the error is $\epsilon_{\mathrm{SWR}} = \epsilon\mathrm{SWR}_{\mathrm{instr}}$.

At locations where long time series of PIRATA downward longwave radiation (dLWR) are available, the error is estimated as the RMS difference between daily PIRATA dLWR and ERA-Interim dLWR for each calendar month, across all years ($\epsilon\mathrm{LWR}_{\mathrm{fill}}$). Otherwise, we use the RMS difference from 0°, 23°W for the other equatorial locations; 10°S, 10°W for 6°S, 10°W; 15°N, 38°W for all other locations along 38°W and 23°W; and 19°S, 34°W for 8°S, 30°W and 14°S, 32°W. An instrumental error of 1% is applied only when PIRATA data are available ($\epsilon\mathrm{LWR}_{\mathrm{instr.}}$). The total error in dLWR is calculated as $\epsilon_{\mathrm{dLWR}} = \sqrt{\epsilon\mathrm{LWR}_{\mathrm{instr.}}^2 + \epsilon\mathrm{LWR}_{\mathrm{fill}}^2}$ on days in which ERA-Interim values are used and $\epsilon_{\mathrm{dLWR}} = \epsilon\mathrm{LWR}_{\mathrm{instr.}}$ is calculated on days in which direct PIRATA measurements are available. The total error in net LWR is given as $\epsilon_{\mathrm{LWR}} = \sqrt{\epsilon_{\mathrm{dLWR}}^2 + \epsilon_{\mathrm{uLWR}}^2}$, where ϵ_{uLWR} is the error in emitted LWR calculated from the SST error and using standard error propagation.

For air temperature, relative humidity, and winds, errors include 1) the RMS difference between daily PIRATA and ERA-Interim values for a given calendar month, based on days when PIRATA data are available at a given location; and 2) instrumental errors of 0.2°C for air temperature, 2.7% for relative humidity, and $0.3\,\mathrm{m\,s^{-1}}$ for wind velocity and speed. On days with missing PIRATA data, the errors are calculated as the square root of the sum of the squares of the RMS error and the instrumental error; on days with PIRATA measurements, the error is equal to the instrumental error.

Uncertainties for the heat and temperature budget terms are calculated using standard error propagation and assuming that the different sources of error for a given term are uncorrelated in time. Error estimates for latent and sensible heat fluxes take into account the errors in air temperature, relative humidity, wind speed, and SST described earlier in the appendix, as well as uncertainty associated with the use of a bulk equation (12% of the daily latent or sensible heat flux value; Fairall et al. 1996b). Typical errors for daily latent, sensible, longwave, and absorbed shortwave heat fluxes are 15–30, 2–7, 5–10, and $5\text{–}20\,\mathrm{W\,m^{-2}}$, respectively. Relative errors (record-length mean daily error divided by mean value) are 10%–30% for latent and longwave, 30%–100% for sensible, and 5%–10% for absorbed shortwave. Daily errors for horizontal heat advection are normally $30\text{–}80\,\mathrm{W\,m^{-2}}$, with maximum values where mixed-layer currents are strongest (along the equator and at 4°N). Because of weak annual mean advection and significant short-time-scale fluctuations at most locations, relative errors can reach as high as 50 times the record-length mean, especially within 4° of the equator.

REFERENCES

Balmaseda, M. A., K. Mogensen, and A. T. Weaver, 2013: Evaluation of the ECMWF ocean reanalysis system ORAS4. *Quart. J. Roy. Meteor. Soc.*, **139**, 1132–1161, https://doi.org/10.1002/qj.2063.

Bombardi, R. J., L. M. V. Carvalho, C. Jones, and M. S. Reboita, 2014: Precipitation over eastern South America and the South Atlantic Sea surface temperature during neutral ENSO periods. *Climate Dyn.*, **42**, 1553–1568, https://doi.org/10.1007/s00382-013-1832-7.

Bonjean, F., and G. S. E. Lagerloef, 2002: Diagnostic model and analysis of the surface currents in the tropical Pacific Ocean. *J. Phys. Oceanogr.*, **32**, 2938–2954, https://doi.org/10.1175/1520-0485(2002)032<2938:DMAAOT>2.0.CO;2.

Bourlès, B., and Coauthors, 2008: The PIRATA program: History, accomplishments, and future directions. *Bull. Amer. Meteor. Soc.*, **89**, 1111–1125, https://doi.org/10.1175/2008BAMS2462.1.

Breugem, W.-P., P. Chang, C. J. Jang, J. Mignot, and W. Hazeleger, 2008: Barrier layers and tropical Atlantic SST biases in coupled GCMs. *Tellus*, **60A**, 885–897, https://doi.org/10.1111/j.1600-0870.2008.00343.x.

Carton, J. A., and B. H. Huang, 1994: Warm events in the tropical Atlantic. *J. Phys. Oceanogr.*, **24**, 888–903, https://doi.org/10.1175/1520-0485(1994)024<0888:WEITTA>2.0.CO;2.

Chiang, J. C. H., and D. J. Vimont, 2004: Analogous Pacific and Atlantic meridional modes of tropical atmosphere–ocean variability. *J. Climate*, **17**, 4143–4158, https://doi.org/10.1175/JCLI4953.1.

——, Y. Kushnir, and A. Giannini, 2002: Deconstructing Atlantic intertropical convergence zone variability: Influence of the local cross-equatorial sea surface temperature gradient and remote forcing from the eastern equatorial Pacific. *J. Geophys. Res.*, **107**, 4004, https://doi.org/10.1029/2000JD000307.

Coles, V. J., M. T. Brooks, J. Hopkins, M. R. Stukel, P. L. Yager, and R. R. Hood, 2013: The pathways and properties of the Amazon River Plume in the tropical North Atlantic Ocean. *J. Geophys. Res. Oceans*, **118**, 6894–6913, https://doi.org/10.1002/2013JC008981.

Cronin, M. F., and W. S. Kessler, 2009: Near-surface shear flow in the tropical Pacific cold tongue front. *J. Phys. Oceanogr.*, **39**, 1200–1215, https://doi.org/10.1175/2008JPO4064.1.

Da-Allada, C. Y., G. Alory, Y. du Penhoat, E. Kestenare, F. Durand, and N. M. Hounkonnou, 2013: Seasonal mixed-layer salinity balance in the tropical Atlantic Ocean: Mean state and seasonal cycle. *J. Geophys. Res. Oceans*, **118**, 332–345, https://doi.org/10.1029/2012JC008357.

de Boyer Montégut, C., G. Madec, A. S. Fischer, A. Lazar, and D. Iudicone, 2004: Mixed layer depth over the global ocean: An examination of profile data and a profile-based climatology. *J. Geophys. Res.*, **109**, C12003, https://doi.org/10.1029/2004JC002378.

Dee, D. P., and Coauthors, 2011: The ERA-Interim reanalysis: Configuration and performance of the data assimilation system. *Quart. J. Roy. Meteor. Soc.*, **137**, 553–597, https://doi.org/10.1002/qj.828.

Ebuchi, N., H. C. Graber, and M. J. Caruso, 2002: Evaluation of wind vectors observed by QuikSCAT/SeaWinds using ocean buoy data. *J. Atmos. Oceanic Technol.*, **19**, 2049–2062, https://doi.org/10.1175/1520-0426(2002)019<2049:EOWVOB>2.0.CO;2.

Fairall, C. W., E. F. Bradley, J. S. Godfrey, G. A. Wick, J. B. Edson, and G. S. Young, 1996a: Cool-skin and warm-layer effects on sea surface temperature. *J. Geophys. Res.*, **101**, 1295–1308, https://doi.org/10.1029/95JC03190.

——, ——, D. P. Rogers, J. B. Edson, and G. S. Young, 1996b: Bulk parameterization of air-sea fluxes for Tropical Ocean-Global Atmosphere Coupled Ocean-Atmosphere Response Experiment. *J. Geophys. Res.*, **101**, 3747–3764, https://doi.org/10.1029/95JC03205.

——, ——, J. E. Hare, A. A. Grachev, and J. B. Edson, 2003: Bulk parameterization of air–sea fluxes: Updates and verification for the COARE algorithm. *J. Climate*, **16**, 571–591, https://doi.org/10.1175/1520-0442(2003)016<0571:BPOASF>2.0.CO;2.

Foltz, G. R., and M. J. McPhaden, 2009: Impact of barrier layer thickness on SST in the central tropical North Atlantic. *J. Climate*, **22**, 285–299, https://doi.org/10.1175/2008JCLI2308.1.

——, S. A. Grodsky, J. A. Carton, and M. J. McPhaden, 2003: Seasonal mixed layer heat budget of the tropical Atlantic Ocean. *J. Geophys. Res.*, **108**, 3146, https://doi.org/10.1029/2002JC001584.

——, M. J. McPhaden, and R. Lumpkin, 2012: A strong Atlantic meridional mode event in 2009: The role of mixed layer dynamics. *J. Climate*, **25**, 363–380, https://doi.org/10.1175/JCLI-D-11-00150.1.

——, C. Schmid, and R. Lumpkin, 2013a: Seasonal cycle of the mixed layer heat budget in the northeastern tropical Atlantic Ocean. *J. Climate*, **26**, 8169–8188, https://doi.org/10.1175/JCLI-D-13-00037.1.

——, A. T. Evan, H. P. Freitag, S. Brown, and M. J. McPhaden, 2013b: Dust accumulation biases in PIRATA shortwave radiation records. *J. Atmos. Oceanic Technol.*, **30**, 1414–1432, https://doi.org/10.1175/JTECH-D-12-00169.1.

——, C. Schmid, and R. Lumpkin, 2015: Transport of surface freshwater from the equatorial to the subtropical North Atlantic Ocean. *J. Phys. Oceanogr.*, **45**, 1086–1102, https://doi.org/10.1175/JPO-D-14-0189.1.

Freitag, H. P., M. E. McCarty, C. Nosse, R. Lukas, M. J. McPhaden, and M. F. Cronin, 1999: COARE Seacat data: Calibrations and quality control procedures. NOAA Tech. Memo. ERL PMEL-115, 89 pp.

Gentemann, C. L., F. J. Wentz, C. A. Mears, and D. K. Smith, 2004: In situ validation of Tropical Rainfall Measuring Mission microwave sea surface temperatures. *J. Geophys. Res.*, **109**, C04021, https://doi.org/10.1029/2003JC002092.

Giarolla, E., P. Nobre, M. Malagutti, and L. P. Pezzi, 2005: The Atlantic Equatorial Undercurrent: PIRATA observations and simulations with GFDL Modular Ocean Model at CPTEC. *Geophys. Res. Lett.*, **32**, L10617, https://doi.org/10.1029/2004GL022206.

Giordani, H., and G. Caniaux, 2014: Lagrangian sources of frontogenesis in the equatorial Atlantic front. *Climate Dyn.*, **43**, 3147–3162, https://doi.org/10.1007/s00382-014-2293-3.

Grodsky, S. A., J. A. Carton, C. Provost, J. Servain, J. A. Lorenzzetti, and M. J. McPhaden, 2005: Tropical instability waves at 0°N, 23°W in the Atlantic: A case study using Pilot Research Moored Array in the Tropical Atlantic (PIRATA) mooring data. *J. Geophys. Res.*, **110**, C08010, https://doi.org/10.1029/2005JC002941.

Ham, Y.-G., J.-S. Kug, J.-Y. Park, and F.-F. Jin, 2013: Sea surface temperature in the north tropical Atlantic as a trigger for El Niño/Southern Oscillation events. *Nat. Geosci.*, **6**, 112–116, https://doi.org/10.1038/ngeo1686.

Han, W., P. J. Webster, J.-L. Lin, W. T. Liu, R. Fu, D. Yuan, and A. Hu, 2008: Dynamics of intraseasonal sea level and thermocline variability in the equatorial Atlantic during 2002–03. *J. Phys. Oceanogr.*, **38**, 945–967, https://doi.org/10.1175/2008JPO3854.1.

Hummels, R., M. Dengler, and B. Bourlès, 2013: Seasonal and regional variability of upper ocean diapycnal heat flux in the Atlantic cold tongue. *Prog. Oceanogr.*, **111**, 52–74, https://doi.org/10.1016/j.pocean.2012.11.001.

——, ——, P. Brandt, and M. Schlundt, 2014: Diapycnal heat flux and mixed layer heat budget within the Atlantic cold tongue. *Climate Dyn.*, **43**, 3179–3199, https://doi.org/10.1007/s00382-014-2339-6.

Jackett, D. R., and T. J. McDougall, 1995: Minimal adjustment of hydrographic profiles to achieve static stability. *J. Atmos. Oceanic Technol.*, **12**, 381–389, https://doi.org/10.1175/1520-0426(1995)012<0381:MAOHPT>2.0.CO;2.

Jouanno, J., F. Marin, Y. du Penhoat, J. Sheinbaum, and J. M. Molines, 2011: Seasonal heat balance in the upper 100 m of the equatorial Atlantic Ocean. *J. Geophys. Res.*, **116**, C09003, https://doi.org/10.1029/2010JC006912.

Kawai, Y., H. Kawamura, S. Takahashi, K. Hosoda, H. Murakami, K. Misako, and L. Guan, 2006: Satellite-based high-resolution global optimum interpolation sea surface temperature data. *J. Geophys. Res.*, **111**, C06016, https://doi.org/10.1029/2005JC003313.

Kossin, J. P., and D. J. Vimont, 2007: A more general framework for understanding Atlantic hurricane variability and trends. *Bull. Amer. Meteor. Soc.*, **88**, 1767–1781, https://doi.org/10.1175/BAMS-88-11-1767.

Kucharski, F., A. Bracco, J. H. Yoo, and F. Molteni, 2007: Low-frequency variability of the Indian monsoon–ENSO relationship and the tropical Atlantic: The weakening of the 1980s and 1990s. *J. Climate*, **20**, 4255–4266, https://doi.org/10.1175/JCLI4254.1.

Lake, B. J., S. M. Noor, H. P. Freitag, and M. J. McPhaden, 2003: Calibration procedures and instrumental accuracy estimates of ATLAS air temperature and relative humidity measurements. NOAA Tech. Memo. OAR PMEL-123, 23 pp.

Lefèvre, N., D. Veleda, M. Araujo, and G. Caniaux, 2016: Variability and trends of carbon parameters at a time series in the eastern tropical Atlantic. *Tellus*, **68B**, 30 305, https://doi.org/10.3402/tellusb.v68.30305.

Locarnini, R. A., and Coauthors, 2013: *Temperature*. Vol. 1, *World Ocean Atlas 2013*, NOAA Atlas NESDIS 73, 40 pp.

Lumpkin, R., and S. Garzoli, 2011: Interannual to decadal changes in the western South Atlantic's surface circulation. *J. Geophys. Res.*, **116**, C01014, https://doi.org/10.1029/2010JC006285.

McPhaden, M. J., 1982: Variability in the central equatorial Indian Ocean. Part II: Oceanic heat and turbulent energy balance. *J. Mar. Res.*, **40**, 403–419.

Mitchell, T. P., and J. M. Wallace, 1992: The annual cycle in equatorial convection and sea surface temperature. *J. Climate*, **5**, 1140–1156, https://doi.org/10.1175/1520-0442(1992)005<1140:TACIEC>2.0.CO;2.

Moisan, J. R., and P. P. Niiler, 1998: The seasonal heat budget of the North Pacific: Net heat flux and heat storage rates (1950–1990). *J. Phys. Oceanogr.*, **28**, 401–421, https://doi.org/10.1175/1520-0485(1998)028<0401:TSHBOT>2.0.CO;2.

Morel, A., and D. Antoine, 1994: Heating rate within the upper ocean in relation to its biooptical state. *J. Phys. Oceanogr.*, **24**, 1652–1665, https://doi.org/10.1175/1520-0485(1994)024<1652:HRWTUO>2.0.CO;2.

Moum, J. N., J. D. Nash, and W. D. Smyth, 2011: Narrowband oscillations in the upper-equatorial ocean. Part I: Interpretation as shear instabilities. *J. Phys. Oceanogr.*, **41**, 397–410, https://doi.org/10.1175/2010JPO4450.1.

——, A. Perlin, J. D. Nash, and M. J. McPhaden, 2013: Seasonal sea surface cooling in the equatorial Pacific cold tongue controlled by ocean mixing. *Nature*, **500**, 64–67, https://doi.org/10.1038/nature12363.

Niiler, P. P., and E. B. Kraus, 1977: One-dimensional models of the upper ocean. *Modelling and Prediction of the Upper Layers of the Ocean*, E. B. Kraus, Ed., Pergamon, 143–172.

Nobre, C., and J. Shukla, 1996: Variation of sea surface temperature, wind stress, and rainfall over the tropical Atlantic and South America. *J. Climate*, **9**, 2464–2479, https://doi.org/10.1175/1520-0442(1996)009<2464:VOSSTW>2.0.CO;2.

Nobre, P., R. A. De Almeida, M. Malagutti, and E. Giarolla, 2012: Coupled ocean–atmosphere variations over the South Atlantic Ocean. *J. Climate*, **25**, 6349–6358, https://doi.org/10.1175/JCLI-D-11-00444.1.

Ohlmann, J. C., 2003: Ocean radiant heating in climate models. *J. Climate*, **16**, 1337–1351, https://doi.org/10.1175/1520-0442-16.9.1337.

Okumura, Y., and S.-P. Xie, 2004: Interaction of the Atlantic equatorial cold tongue and the African monsoon. *J. Climate*, **17**, 3589–3602, https://doi.org/10.1175/1520-0442(2004)017<3589:IOTAEC>2.0.CO;2.

——, and ——, 2006: Some overlooked features of tropical Atlantic climate leading to a new Niño-like phenomenon. *J. Climate*, **19**, 5859–5874, https://doi.org/10.1175/JCLI3928.1.

Parard, G., J. Boutin, Y. Cuypers, P. Bouruet-Aubertot, and G. Caniaux, 2014: On the physical and biogeochemical processes driving the high frequency variability of CO_2 fugacity at 6°S, 10°W: Potential role of the internal waves. *J. Geophys. Res. Oceans*, **119**, 8357–8374, https://doi.org/10.1002/2014JC009965.

Payne, R. E., 1972: Albedo of the sea surface. *J. Atmos. Sci.*, **29**, 959–970, https://doi.org/10.1175/1520-0469(1972)029<0959:AOTSS>2.0.CO;2.

Peter, A. C., M. Le Henaff, Y. Du Penhoat, C. E. Menkes, F. Marin, J. Vialard, G. Caniaux, and A. Lazar, 2006: A model study of the seasonal mixed layer heat budget in the equatorial Atlantic. *J. Geophys. Res.*, **111**, C06014, doi:10.1029/2005JC003157.

Pham, H. T., S. Sarkar, and K. B. Winters, 2013: Large-eddy simulation of deep-cycle turbulence in an Equatorial Undercurrent model. *J. Phys. Oceanogr.*, **43**, 2490–2502, https://doi.org/10.1175/JPO-D-13-016.1.

Polo, I., B. Rodríguez-Fonseca, T. Losada, and J. Garcia-Serrano, 2008: Tropical Atlantic variability modes (1979–2002). Part I: Time-evolving SST modes related to West African rainfall. *J. Climate*, **21**, 6457–6475, https://doi.org/10.1175/2008JCLI2607.1.

Praveen Kumar, B., J. Vialard, M. Lengaigne, V. S. N. Murty, and M. J. McPhaden, 2012: TropFlux: Air-sea fluxes for the global tropical oceans—Description and evaluation. *Climate Dyn.*, **38**, 1521–1543, https://doi.org/10.1007/s00382-011-1115-0.

Reul, N., Y. Quilfen, B. Chapron, S. Fournier, V. Kudryavtsev, and R. Sabia, 2014: Multisensor observations of the Amazon-Orinoco river plume interactions with hurricanes. *J. Geophys. Res. Oceans*, **119**, 8271–8295, https://doi.org/10.1002/2014JC010107.

Reynolds, R. W., and T. M. Smith, 1994: Improved global sea surface temperature analyses using optimum interpolation. *J. Climate*, **7**, 929–948, https://doi.org/10.1175/1520-0442(1994)007<0929:IGSSTA>2.0.CO;2.

Richter, I., and S.-P. Xie, 2008: On the origin of equatorial Atlantic biases in coupled general circulation models. *Climate Dyn.*, **31**, 587–598, https://doi.org/10.1007/s00382-008-0364-z.

Rodríguez-Fonseca, B., I. Polo, J. García-Serrano, T. Losada, E. Mohino, C. R. Mechoso, and F. Kucharski, 2009: Are Atlantic Niños enhancing Pacific ENSO events in recent decades? *Geophys. Res. Lett.*, **36**, L20705, https://doi.org/10.1029/2009GL040048.

Rouault, M., J. Servain, C. J. C. Reason, B. Bourlès, M. J. Rouault, and N. Fauchereau, 2009: Extension of PIRATA in the tropical Southeast Atlantic: An initial one-year experiment. *Afr. J. Mar. Sci.*, **31**, 63–71, https://doi.org/10.2989/AJMS.2009.31.1.5.776.

Rugg, A., G. R. Foltz, and R. C. Perez, 2016: Role of mixed layer dynamics in tropical North Atlantic interannual sea surface temperature variability. *J. Climate*, **29**, 8083–8101, https://doi.org/10.1175/JCLI-D-15-0867.1.

Serra, Y. L., and M. J. McPhaden, 2003: Multiple time- and space-scale comparisons of ATLAS buoy rain gauge measurements with TRMM satellite precipitation measurements. *J. Appl. Meteor.*, **42**, 1045–1059, https://doi.org/10.1175/1520-0450(2003)042<1045:MTASCO>2.0.CO;2.

Servain, J., and Coauthors, 1998: A Pilot Research Moored Array in the Tropical Atlantic (PIRATA). *Bull. Amer. Meteor. Soc.*, **79**, 2019–2031, https://doi.org/10.1175/1520-0477(1998)079<2019:APRMAI>2.0.CO;2.

Smyth, W. D., J. N. Moum, L. Li, and S. A. Thorpe, 2013: Diurnal shear instability, the descent of the surface shear layer, and the deep cycle of equatorial turbulence. *J. Phys. Oceanogr.*, **43**, 2432–2455, https://doi.org/10.1175/JPO-D-13-089.1.

Stevenson, J. W., and P. P. Niiler, 1983: Upper ocean heat budget during the Hawaii-to-Tahiti Shuttle Experiment. *J. Phys. Oceanogr.*, **13**, 1894–1907, https://doi.org/10.1175/1520-0485(1983)013<1894:UOHBDT>2.0.CO;2.

Sweeney, C., A. Gnanadesikan, S. M. Griffies, M. J. Harrison, A. J. Rosati, and B. L. Samuels, 2005: Impacts of shortwave penetration depth on large-scale ocean circulation and heat transport. *J. Phys. Oceanogr.*, **35**, 1103–1119, https://doi.org/10.1175/JPO2740.1.

Wade, M., G. Caniaux, Y. DuPenhoat, M. Dengler, H. Giordani, and R. Hummels, 2011: A one-dimensional modeling study of the diurnal cycle in the equatorial Atlantic at the PIRATA buoys during the EGEE-3 campaign. *Ocean Dyn.*, **61**, 1–20, https://doi.org/10.1007/s10236-010-0337-8.

Wenegrat, J. O., and M. J. McPhaden, 2015: Dynamics of the surface layer diurnal cycle in the equatorial Atlantic Ocean (0°, 23°W). *J. Geophys. Res. Oceans*, **120**, 563–581, https://doi.org/10.1002/2014JC010504.

Woodruff, S., and Coauthors, 2011: ICOADS Release 2.5: Extensions and enhancements to the surface marine meteorological archive. *Int. J. Climatol.*, **31**, 951–967, https://doi.org/10.1002/joc.2103.

Yoon, J.-H., and N. Zeng, 2010: An Atlantic influence on Amazon rainfall. *Climate Dyn.*, **34**, 249–264, https://doi.org/10.1007/s00382-009-0551-6.

Yu, L., and R. A. Weller, 2007: Objectively analyzed air–sea heat fluxes for the global ice-free oceans (1981–2005). *Bull. Amer. Meteor. Soc.*, **88**, 527–539, https://doi.org/10.1175/BAMS-88-4-527.

——, X. Jin, and R. A. Weller, 2006: Role of net surface heat flux in seasonal variations of sea surface temperature in the tropical Atlantic Ocean. *J. Climate*, **19**, 6153–6169, https://doi.org/10.1175/JCLI3970.1.

Zebiak, S., 1993: Air–sea interaction in the equatorial Atlantic region. *J. Climate*, **6**, 1567–1586, https://doi.org/10.1175/1520-0442(1993)006<1567:AIITEA>2.0.CO;2.

Zweng, M. M., and Coauthors, 2013: *Salinity*. Vol. 2, *World Ocean Atlas 2013*, NOAA Atlas NESDIS 74, 39 pp.